POLITECNICO DI TORINO
Repository ISTITUZIONALE

Andreev spin qubits based on the helical edge states of magnetically doped two-dimensional topological insulators

Original
Andreev spin qubits based on the helical edge states of magnetically doped two-dimensional topological insulators / Latini, E., Rossi, F., Dolcini, F.. - In: PHYSICAL REVIEW RESEARCH. - ISSN 2643-1564. - STAMPA. - 8:3(2026), pp. 1-18. [10.1103/jwtl-dz3v]

Availability:
This version is available at: 11583/3015087 since: 2026-09-02T08:19:29Z

Publisher:
American Physical Society - APS

Published
DOI:10.1103/jwtl-dz3v

Terms of use:

This article is made available under terms and conditions as specified in the corresponding bibliographic description in the repository

Publisher copyright

(Article begins on next page)

26 November 2026

Andreev spin qubits based on the helical edge states of magnetically doped two-dimensional topological insulators

Edoardo Latini,* Fausto Rossi,† and Fabrizio Dolcini‡
Dipartimento di Scienza Applicata e Tecnologia del Politecnico di Torino, I-10129 Torino, Italy

(Received 3 February 2026; accepted 17 July 2026; published 17 August 2026)

We show that Andreev spin qubits can be realized in a Josephson junction based on the helical edge states of a two-dimensional topological insulator (quantum spin Hall system) proximized by superconducting films, in the presence of magnetic doping. We demonstrate that the electric dipole transitions between the Andreev spin states induced by the magnetic doping can be harnessed to manipulate the Andreev spin qubit by microwave radiation pulses, without applying an external Zeeman field or invoking ancillary states. We numerically simulate the realization of NOT and Hadamard quantum logic gates, and discuss implementations in realistic setups.

DOI: 10.1103/jwtl-dz3v

I. INTRODUCTION

Andreev spin qubits (ASQs) represent one of the most promising proposals of solid-state platforms for quantum information processing. In an ASQ, a doublet of spin-split Andreev bound states (ABSs) is designed through a Josephson junction (JJ) where the weak link is characterized by spin-orbit coupling [1,2]. As compared to qubit realizations based on conventional quantum dots, an ASQ exhibits several compelling benefits. The discrete ABSs emerge from the superconductor gap rather than electrical confinement, making electron-electron interaction effects negligible. Moreover, the readout of the ASQ quantum state can be achieved by measuring the dissipationless current flowing through the JJ [3–5]. Finally, the spin degree of freedom is usually expected to be more robust to environmental decoherence than charge [6,7], and spin-flip error correction architectures have also been recently proposed [8].

So far, implementations of ASQs have been theoretically investigated [9–11] and experimentally realized [8,12–19] mainly in semiconductor nanowires with strong spin-orbit coupling contacted to two superconducting banks. Evidence of the resulting spin-split ABSs in the weak link was observed, and the possibility to control, read out, and manipulate the spin qubit via microwave radiation was in principle demonstrated [8,13–19]. However, in view of scalable quantum architectures a major limitation of this platform is the relatively short decoherence time (tens of nanoseconds) arising from a spin noisy environment. This is attributed to the fact that the nanowire weak link is typically based on Indium (e.g., InAs), an element characterized by a large nuclear spin, which via hyperfine interaction acts as a spin bath causing decoherence on the ASQ [14,15,18–20].

During the past year, various strategies to circumvent these difficulties have been proposed. On the one hand, it has been argued that replacing InAs nanowires with a germanium two-dimensional hole gas could reduce decoherence by isotopic purification [21]. However, the realization of Ge-based JJs is quite recent and, at the moment, is limited to planar junctions [22,23], which do not exhibit discrete ABSs. On the other hand, spin relaxation is predicted to be suppressed by shunting the ASQ with a capacitor, but only provided that the conditions for the Franck-Condon blockade are fulfilled [24]. Other proposals for ASQs require external magnetic field [25] or *ad hoc* configurations such as three-terminal devices [26] or Corbino geometries [27]. Thus, the search for a convincing alternative to the nanowire implementation of ASQs still remains a challenging open problem.

Here, we propose a quite different strategy to attack this problem, based on a JJ realized with a two-dimensional topological insulator, namely, a quantum spin Hall insulator (QSHI) [28–31]. This peculiar state of matter has been experimentally observed in HgTe/CdTe [32–35] quantum wells, in InAs/GaSb [36,37] bilayers, Bi bilayers [38–40], as well as in WTe_2 monolayers [41–43]. Notably, not only a QSHI-based platform for ASQ is realistic, but it also exhibits intrinsic advantages as compared to current implementation relying on conventional materials. First, since spin-orbit coupling is the effect underlying the topological transition in these systems, the topological edge states are helical, namely, their propagation direction is locked to the spin orientation. As a consequence, the ABSs emerging in a helical JJ are naturally spin split, providing a built-in platform to realize ASQs. Second, the electronic conducting states emerging at the boundaries of a QSHI are extremely robust to perturbations. Indeed, besides being topologically protected from elastic time-reversal disorder effects [28–32], they are also effectively robust to inelastic phonon coupling [44,45], and

*Contact author: edoardo.latini@polito.it
†Contact author: fausto.rossi@polito.it
‡Contact author: fabrizio.dolcini@polito.it

Published by the American Physical Society under the terms of the Creative Commons Attribution 4.0 International license. Further distribution of this work must maintain attribution to the author(s) and the published article's title, journal citation, and DOI.

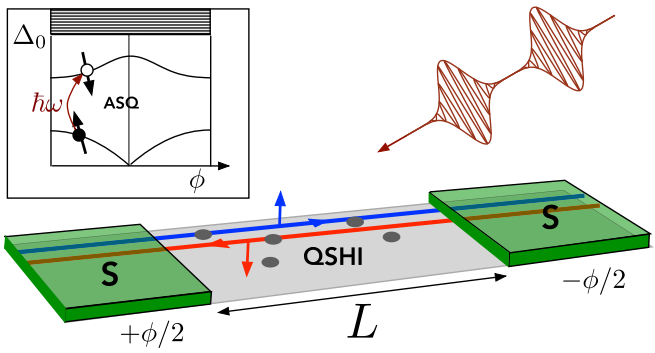

FIG. 1. Scheme of realization of an ASQ based on a two-dimensional topological insulator: A helical Josephson junction realized by proximizing the helical edge states of a QSHI with s-wave superconducting (S) films. The presence of magnetic doping (black spots) induces electric dipole transitions between the ABSs localized in the weak link (inset), enabling the control of the qubit via coupling with an electromagnetic radiation.

their hyperfine interaction is small, especially in HgTe implementations [46–49]. Moreover, JJs based on QSHI have already been realized in various experiments [50–55] and are state-of-the-art technology by now.

The manipulation of an ASQ is customarily performed via coupling to a microwave radiation. However, as is well known, electric dipole transitions between helical-based ABSs are *a priori* forbidden by selection rules imposed by their very helical nature [56–58]. Magnetic dipole transitions, relying on the Zeeman coupling with circularly polarized radiation [56,59], are typically very weak and would not be suitable to enable fast operations on an ASQ. The recently realized magnetic doping of two-dimensional topological insulators might turn the tide in this respect [54,60,61]. The effects of magnetic impurities on QSHI have been analyzed in various contexts, such as the realization of quantum anomalous Hall effect [62,63], the localization of Majorana quasiparticles [64], and their interplay with Coulomb interaction [65–70]. However, as we shall show, when a QSHI is embedded in a JJ, the presence of magnetic impurities also alters the spin texture of the ABSs, leading to nonvanishing electric dipole transition amplitudes and thereby opening up the possibility to manipulate the ASQ with a microwave radiation. The scheme of the proposed setup is depicted in Fig. 1. A JJ, realized by proximizing a pair of counterpropagating helical states of a QSHI with two s-wave superconductors, hosts ABS localized within the weak link of length L (see the inset). The ABSs are spin nondegenerate, due to the helical nature of the edge states, and realize the ASQ. The dark spots present in Fig. 1 along the edge describe magnetic impurities, while radiation pulses applied on the weak link enable one to control the ASQ.

The paper is organized as follows. In Sec. II, we present the model for the ASQ, the resulting ABSs and their spin texture. Then, in Sec. III, we analyze the coupling of the ASQ to an electromagnetic radiation, and present a detailed study of the electric dipole transition amplitude as a function of the spatial extension of the doping and the transparency of the junction. Then, in Sec. IV, we present our results about the manipulation of the ASQ, showing that it is possible to implement the NOT and Hadamard quantum gates by suitably applied electromagnetic pulses. We discuss our results in Sec. V, where we propose possible experimental realizations with state-of-the-art technology; we address the quantum state preparation and the dissipation and decoherence effects. Finally, in Sec. VI, we draw our conclusions.

II. THE MODEL

A. Hamiltonian of the system

We consider a pair of one-dimensional counterpropagating states flowing along the edge of a QSHI. As is customary, within the bulk gap of the topological insulator, the spectrum of the edge states can reliably be assumed to be linear and characterized by a Fermi velocity v_F [29,65]. Moreover, the helical nature of such topological edge states implies that their spin orientation is locked to the propagation direction. For definiteness, we shall assume that right- and left-moving electrons are characterized by spin-$\uparrow$ and spin-$\downarrow$, respectively, and are described by the massless Dirac fermion Hamiltonian in $1+1$ dimensions

$$\mathcal{H}_{\rm hel} = \int dx\ (\psi_\uparrow^\dagger, \psi_\downarrow^\dagger)\,(v_F p_x \sigma_z - \mu\sigma_0)\begin{pmatrix}\psi_\uparrow\\ \psi_\downarrow\end{pmatrix}, \qquad (1)$$

where $\psi_\uparrow(x)$ and $\psi_\downarrow(x)$ denote the electron field operators, $p_x = -i\hbar\partial_x$ is the momentum operator, σ_z is the Pauli matrix acting on spin space, and μ is the chemical potential.

The deposition of two s-wave superconducting films on the QSHI induces by proximity effect a superconducting pairing along the two helical regions underneath, which are separated by a mesoscopic weak link of nonproximized helical states, with a length L, as depicted in Fig. 1. The resulting superconducting pairing is described by the Hamiltonian term

$$\mathcal{H}_{\rm SC} = \int dx\,(\Delta(x)\,\psi_\uparrow^\dagger\psi_\downarrow^\dagger + \Delta^*(x)\psi_\downarrow\psi_\uparrow), \qquad (2)$$

where

$$\Delta(x) = \Delta_0\begin{cases} e^{i\phi/2}, & x < -L/2,\\ 0, & |x| < L/2,\\ e^{-i\phi/2}, & x > +L/2.\end{cases} \qquad (3)$$

Here, $\Delta_0 > 0$ is the magnitude of the induced pairing, while ϕ denotes the superconducting phase difference.

The presence of a magnetic disorder inside the weak link is accounted for by a term

$$\mathcal{H}_M = \int dx\ (\psi_\uparrow^\dagger, \psi_\downarrow^\dagger)\,\mathbf{m}(x)\cdot\boldsymbol{\sigma}\begin{pmatrix}\psi_\uparrow\\ \psi_\downarrow\end{pmatrix}, \qquad (4)$$

where $\boldsymbol{\sigma} = (\sigma_x, \sigma_y, \sigma_z)$ denotes the vector of the three Pauli matrices and $\mathbf{m}(x)$ is a space-dependent magnetization vector. By construction, such term breaks time-reversal symmetry explicitly. However, while the m_z component is parallel to the natural spin orientation z axis of the helical states [see Eq. (1)], the orthogonal m_x and m_y components can induce backscattering of the helical states. As we shall see, this affects the spin texture of the ABSs characterizing the JJ.

By introducing the Nambu spinor $\Psi = (\psi_\uparrow, \psi_\downarrow, \psi_\downarrow^\dagger, -\psi_\uparrow^\dagger)^T$, the Hamiltonian

$$\mathcal{H}_0 = \mathcal{H}_{\rm hel} + \mathcal{H}_{\rm SC} + \mathcal{H}_M \qquad (5)$$

can be rewritten, up to a constant, in the Bogoliubov–de Gennes (BdG) form $\mathcal{H}_0 = (1/2)\int \Psi^\dagger(x) H_{\rm BdG}(x)\Psi(x)\,dx$, where

$$H_{\rm BdG}(x) = \begin{pmatrix} H_e(x) & \Delta(x)\sigma_0 \\ \Delta^*(x)\sigma_0 & H_h(x) \end{pmatrix} \tag{6}$$

is the BdG Hamiltonian, with

$$H_e(x) = v_F\sigma_z p_x - \mu\sigma_0 + \mathbf{m}(x)\cdot\boldsymbol{\sigma}, \tag{7a}$$

$$H_h(x) = -\mathcal{T}H_e\mathcal{T}^{-1} = -\sigma_y(H_e)^*\sigma_y = -v_F\sigma_z p_x + \mu\sigma_0 + \mathbf{m}(x)\cdot\boldsymbol{\sigma} \tag{7b}$$

denoting the electron(e) and hole(h) sector diagonal blocks, respectively. Here, σ_0 is the 2×2 identity matrix in spin space, and $\mathcal{T} = -i\sigma_y K$ is the time-reversal operator, with K denoting the complex conjugation. By reexpressing the Nambu field Ψ in terms of the eigenfunction set $\Phi_i(x)$ of the BdG Hamiltonian (6)

$$\Psi(x) = \sum_{E_i\geqslant 0}(\Phi_i^{(+)}(x)\gamma_i + \Phi_i^{(-)}(x)\gamma_i^\dagger), \tag{8}$$

the Hamiltonian $\mathcal{H}_0$ can be brought to the diagonal form of a two-level system collection

$$\mathcal{H} = \sum_{E_i\geqslant 0} E_i(\phi)\left(\gamma_i^\dagger\gamma_i - \frac{1}{2}\right), \tag{9}$$

with γ_i denoting fermionic Bogoliubov quasiparticle operators. In Eq. (8), $\Phi_i^{(+)}(x) = (u_{\uparrow,i}, u_{\downarrow,i}, v_{\downarrow,i}, v_{\uparrow,i})^T(x)$ denote the eigenfunctions of the BdG Hamiltonian (6) with positive eigenvalues $E_i \geqslant 0$ (discrete and continuous spectrum), while $\Phi_i^{(-)}(x) = (\tau_y\otimes\sigma_y)(\Phi_i^{(+)}(x))^*$ are the charge conjugated of $\Phi_i^{(+)}$ and have energies $-E_i$.

B. Andreev bound states

Due to the helical nature of the QSHI edge states, the ABSs, labeled by $i = 1, \ldots, N$, are nondegenerate in spin. They are characterized by a discrete subgap spectrum $0 \leqslant E_i(\phi) < \Delta_0$ and by wavefunctions $\Phi_i(x)$ localized in the weak link. As is well known, the ABSs can be determined by combining the particle-hole Andreev scattering at the interfaces $x = \pm L/2$ with the normal scattering induced by the magnetic doping present in the weak link [71]. Indeed, any static magnetic disorder with *arbitrary* profile $\mathbf{m}(x)$ can be described in terms of a unitary scattering matrix. Specifically, the electron scattering matrix $S_e(E)$, characterized by transmission amplitudes t_e, t_e' and reflection amplitudes r_e, r_e', can always be expressed in the form

$$S_e(E) = \begin{pmatrix} r_e(E) & t_e'(E) \\ t_e(E) & r_e'(E) \end{pmatrix} = e^{i\Gamma_m(E)}\begin{pmatrix} -i\,e^{+i\Theta_m(E)}\sqrt{1-T_E} & e^{i\chi_m(E)}\sqrt{T_E} \\ e^{-i\chi_m(E)}\sqrt{T_E} & -i\,e^{-i\Theta_m(E)}\sqrt{1-T_E} \end{pmatrix}, \tag{10}$$

where $T_E = |t_e|^2 = |t_e'|^2$ and $R_E = 1 - T_E$ denote the energy-dependent transmission and reflection coefficients, respectively, while Γ_m, Θ_m, and χ_m are complex phase parameters. For holes, the scattering matrix is obtained as

$$S_h(E) = -\sigma_z\, S_e^*(-E)\,\sigma_z. \tag{11}$$

The equation for the ABS energy levels is [64]

$$\cos^2\left[\arccos\frac{E}{\Delta_0} - \frac{EL}{\hbar v_F} - \Gamma_m^A(E)\right] = \frac{1}{2}\big(1 - \sqrt{R_E R_{-E}}\,\cos\big(2\Theta_m^A(E)\big) + \sqrt{T_E T_{-E}}\,\cos\big(\phi - 2\chi_m^S(E)\big)\big), \tag{12}$$

where

$$\Theta_m^A(E) = \tfrac{1}{2}(\Theta_m(E) - \Theta_m(-E)),$$
$$\Gamma_m^A(E) = \tfrac{1}{2}(\Gamma_m(E) - \Gamma_m(-E))m,$$
$$\chi_m^S(E) = \tfrac{1}{2}(\chi_m(E) + \chi_m(-E)) \tag{13}$$

are determined by the parameters characterizing the scattering matrix in Eq. (10).

As compared to the studies on JJs aiming to determine the current-phase relation of the Josephson current, for the present problem of ASQ realizations two important aspects are worth noticing. First, designing a qubit requires to deal with a limited number of ABSs only. Indeed, while at least two ABS are needed to realize a two-level system, the presence of too many levels would be detrimental, for their energy separation would be too small to enable the selective manipulation of the quantum state with a radiation. The number of ABSs is known [72] to depend on the ratio

$$\lambda = \frac{L}{\xi_S} = \frac{\Delta_0}{\hbar v_F/L} \tag{14}$$

of the weak link length L to the superconducting coherence length $\xi_S = \hbar v_F/\Delta_0$. Typically, analytical results can be obtained in the limits of either short junction ($L \ll \xi_S$) [73], where only one ABS is present, or long junction ($L \gg \xi_S$) [74], where many closely spaced energy levels are present. For an ASQ, however, one has to operate in the *intermediate* length regime, where $L \sim \xi_S$, and determine the ABS spectrum $E_i(\phi)$ by solving Eq. (12) numerically. The second relevant aspect is that, while the Josephson current only requires to find the eigenvalues $E_i(\phi)$, modeling an ASQ also implies to determine the ABS *eigenfunctions* $\Phi_i(x)$. Indeed, the manipulation of the ASQ crucially depends on the possibility to induce spin-flip processes, i.e., to control transitions between the two ASQ states. As we shall discuss below in detail, in the QSHI helical states, where charge current is closely related to spin, such transitions are determined by the overlap integrals of the current between pairs of different ABS eigenfunctions $\Phi_i(x)$'s, which in turn are closely related to the matrix entries of the electric dipole. Thus, the manipulation of the ASQ via the coupling to an electromagnetic radiation relies on the possibility to have nonvanishing electric dipole transitions between the ABS. Notably, selection rules play a crucial role in this mechanism.

Indeed, for a clean JJ, the helical nature of the QSHI edge states implies that each ABS wavefunction $\Phi_i(x)$ is an eigenfunction of the z component of the spin operator. One has either spin-$\uparrow$ ABS, i.e., excitations characterized by the

combination of spin-↑ particles and spin-↓ holes, or spin-↓ ABS, i.e., excitations characterized by the combination of spin-↓ particles and spin-↑ holes. In this case, spin selection rules forbid any electric dipole transitions between opposite spin states, and it is not possible to manipulate the ASQ.

The presence of magnetic disorder is the mechanism to circumvent this problem. In order to illustrate how, we first observe that, in terms of spatial distribution, one can have various disorder scenarios, ranging from an extremely dilute disorder, where at most one magnetic impurity occurs within the weak link of the JJ, to a spatially dense disorder, where the weak link hosts a uniform distribution of impurities with randomly oriented magnetizations. Here, our purpose is not to carry out a detailed investigation on the possible disorder configurations or to compare a single sample versus a sample averaging. Rather, we aim to illustrate the basic ingredients leading to manipulate the ASQ in the presence of magnetic disorder. Specifically, the m_x and m_y components that are *orthogonal* to the natural spin orientation axis alter the spin texture of the ABS enabling spin-flip transitions. The simplest model to illustrate this effect is the "magnetic barrier" profile

$$\mathbf{m}(x)\cdot\boldsymbol{\sigma} = \begin{cases} m_\perp \sigma_x, & x_0 - \frac{L_m}{2} < x < x_0 + \frac{L_m}{2}, \\ 0, & \text{otherwise}, \end{cases} \tag{15}$$

where L_m and x_0 denote the length and the center of the magnetic barrier inside the weak link, respectively, while the additional conditions $-L/2 < x_0 - L_m/2$ and $x_0 + L_m/2 < L/2$ ensure that the barrier is inside the weak link. Two cases are noteworthy. The limit of a narrow and high barrier, $L_m \to 0, m_\perp \to \infty$, with keeping the "area" parameter $\alpha = m_\perp L_m/\hbar v_F$ constant, describes the case of spatially dilute disorder, namely, one single δ-like magnetic impurity located at a generic position x_0. In contrast, the case $L_m \to L$ (with $x_0 \to 0$) can effectively mimic the case of magnetic disorder uniformly distributed along the entire weak link (see at the end of this section for more details). For these two limiting cases, the two ABSs present in an intermediate length Josephson junction ($L = 2\xi_S$) are shown by the solid black curve and the dashed red curve depicted in Fig. 2. For a comparison, the dotted blue curve illustrates the ABS in the absence of any magnetic disorder (clean helical JJ). As one can see, the zero-energy crossing of the lower ABS at $\phi = \pi$ is robust to the presence of magnetic disorder. This is known to be a hallmark of a topological JJ [75–79] and is in striking contrast with the behavior of conventional JJs [72].

We emphasize that the ABS wavefunctions Φ_1 and Φ_2 are mutually *orthogonal*, since they are eigenfunctions of the BdG Hamiltonian (6) related to two different eigenvalues E_1 and E_2. Thus, they represent the quantum computational states $|0\rangle$ and $|1\rangle$ of the ASQ. At a given superconducting phase bias ϕ, the energy difference between the two ABSs determines the frequency $\omega = (E_2 - E_1)/\hbar$ of the radiation enabling the manipulation of the ASQ state. As one can see from Fig. 2, such energy difference is maximal for $\phi = \pi$ and minimal at phase difference $\phi = 0, 2\pi$. This might at first suggest that the optimal value of ϕ for ASQ manipulation is π. However, as we shall see in the next section, the electric dipole transition amplitudes depend on ϕ in a way opposite to the energy gap.

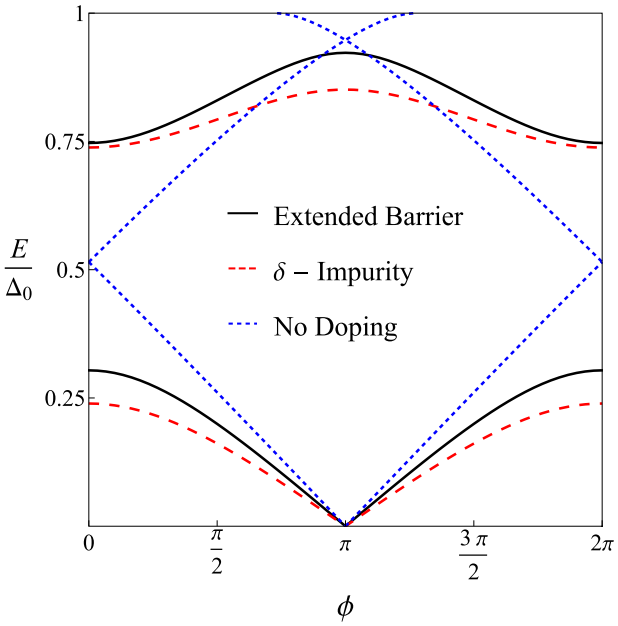

FIG. 2. The ABS energy levels as a function of the superconducting phase difference ϕ are shown for a helical JJ with a length parameter $\lambda = 2$, in the presence of magnetic barrier, characterized by a parameter $\alpha = m_\perp L_m/\hbar v_F = 1$, for chemical potential value $\mu = \Delta_0/2$. The black solid curve and the dashed red curve describe the cases of magnetic disorder extended over the entire weak link ($L_m \to L$) and of a localized magnetic impurity ($L_m \to 0$) located at $x_0 = L/6$, respectively. For comparison, the dotted blue curve depicts the ABS in the absence of any magnetic disorder.

Both these aspects have to be taken into account in investigating the ASQ manipulation.

For each discrete ABS eigenvalue $E_i(\phi)$, we have determined the related eigenfunction $\Phi_i(x)$. While details about the explicit computation are given in Appendix, here we would like to discuss the spatial profile of their spin density, defined as

$$S_\alpha^{(i)}(x) = \Phi_i^\dagger(x)\Sigma_\alpha\Phi_i(x), \quad \alpha = x, y, z, \tag{16}$$

where $\Sigma_\alpha = \tau_0 \otimes \sigma_\alpha$ are the spin operators in Nambu formalism. The result for the case of a JJ with two ABSs Φ_1 and Φ_2 is illustrated in the two panels (a) and (b) of Fig. 3, respectively. In each panel, the dashed vertical dotted lines at $x/L = \pm 1/2$ are a guide to the eye to identify the JJ weak link, and the three solid curves describe the three components S_α of the spin density, in the presence of a magnetic δ impurity located at $\xi_0 = x_0/L$. For a comparison, the dashed curves describe the case of a clean JJ, where S_z is the only nonvanishing component, since the ABS are eigenstates of Σ_z. As one can see, the presence of the magnetic impurity alters the spin texture of the ABS, decreasing the magnitude of the S_z component and introducing a $S_x \neq 0$ component, which exhibits a singularity at the impurity location ξ_0 (marked by a vertical thin dotted line). A scheme to detect the helical state spin texture has been proposed in Ref. [80].

Before concluding this section, we would like to illustrate why the profile (15) is expected to effectively describe the case of uniformly distributed disorder, when $L_m \to L$. We start by

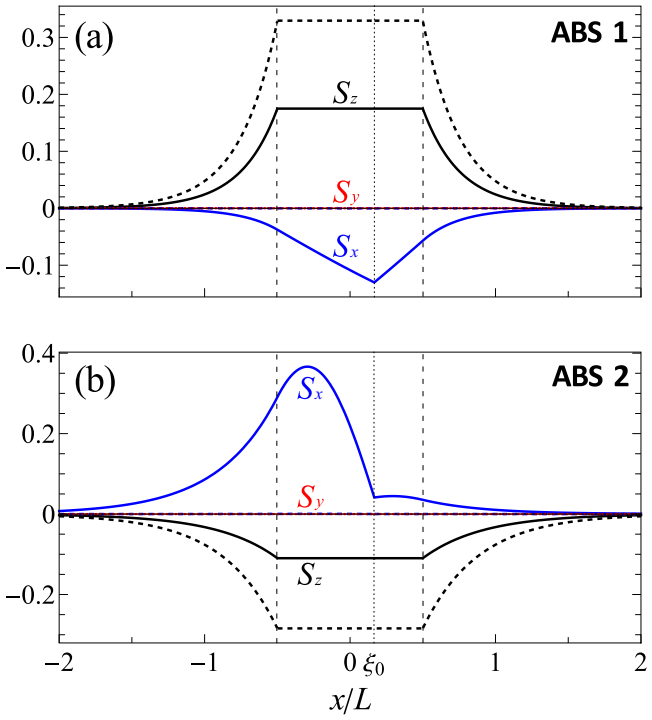

FIG. 3. Spatial profile of the three spin density components S_x, S_y, S_z (in units of $1/L$), for the two ABSs present in a weak link with length parameter $\lambda = 2$. The vertical dashed lines at $x/L = \pm 1/2$ are a guide to the eye to identify the weak link region. The value of the superconducting phase difference is $\phi = \pi/2$. The solid curves refer to the case of the presence of a magnetic δ impurity located at $\xi_0 = x_0/L = 1/6$ and with parameter $\alpha = 1$, while the dashed curves depict, for comparison, the case of a clean JJ without magnetic disorder, where S_z is the only nonvanishing component.

observing that, in the limit of one single isolated impurity, the specific orientation of the magnetization **m** within the x-y plane orthogonal to the natural spin orientation of the helical states is irrelevant: It is just equivalent to a rotation of the spin axes around z. In the case one has a few impurities, quantum interference phenomena between the backscattering processes at the various impurities might arise, depending on the relative impurity distance and the relative orientation of their magnetization in the x-y plane [64]. However, if one considers the case of many impurities that are uniformly distributed along the weak link with random magnetization directions, the quantum interference effects would mutually cancel out, and only the classical (i.e., incoherent) contributions—consisting in the sum of the effects of each individual impurity—would matter. Because for each individual impurity the magnetization orientation is irrelevant, the effective result is expected to be the same when all impurity magnetizations are aligned in the same direction. Thus, a uniform distribution of weak impurities can be mimicked by the uniform magnetization profile (15).

III. COUPLING TO ELECTROMAGNETIC RADIATION AND TRANSITION AMPLITUDES

We now consider a full Hamiltonian

$$\mathcal{H} = \mathcal{H}_0 + \mathcal{H}', \tag{17}$$

where $\mathcal{H}_0$ is given by Eq. (5), while the additional time-dependent term

$$\mathcal{H}' = -\int dx \mathcal{J}(x) A(x,t) \tag{18}$$

describes the coupling of the helical states to an electromagnetic radiation. Here, $A(x,t)$ is the vector potential describing an electric field pulse $E(x,t) = -\partial_t A(x,t)$ in Système International (SI) units, while

$$\begin{aligned}\mathcal{J}(x) &= \mathrm{e} v_F (\psi_\uparrow^\dagger(x)\psi_\uparrow(x) - \psi_\downarrow^\dagger(x)\psi_\downarrow(x)) \\ &= \frac{\mathrm{e}\, v_F}{2} \Psi^\dagger(x)(\tau_0 \otimes \sigma_z)\Psi(x)\end{aligned} \tag{19}$$

is the current density operator, with e denoting the elementary charge and τ_0 the 2×2 identity in Nambu space. Equation (19) explicitly shows that the current operator contains the z component $\Sigma_z = \tau_0 \otimes \sigma_z$ of the spin operator in Nambu formalism. This implies that, differently from conventional materials, the spin texture of the ABS realized with QSHI edge states matters in determining interlevel transitions induced by the coupling (18).

We shall now make the following assumptions. First, since the subterahertz frequency range related to the typical superconducting gap $\Delta_0 \lesssim 1$ meV corresponds to a wavelength of a few millimeters, i.e., far larger than the typical length $L \lesssim 1\,\mu$m of the junction, the electromagnetic pulse can be assumed to be spatially uniform, and the coupling term (18) can be approximated to

$$\mathcal{H}' \simeq -A(t) \int dx\, \mathcal{J}(x)\,. \tag{20}$$

The second assumption is that, since the physical processes relevant to the ASQ occur in the energy range $0 \leqslant E < \Delta_0$ within the superconducting gap Δ_0, the expansion (8) of the electron field operator in terms of all the eigenfunctions of the Bogoliubov–de Gennes equations can be well approximated by retaining only the N discrete ABS solutions, and neglecting the contribution from the continuum states ($E > \Delta_0$):

$$\Psi(x) \simeq \sum_{0 \leqslant E_j \leqslant \Delta_0} (\Phi_j^{(+)}(x)\gamma_j + \Phi_j^{(-)}(x)\gamma_j^\dagger)\,. \tag{21}$$

This reduces the dimensionality of the problem to the essential degrees of freedom needed for the ASQ manipulation. Inserting Eq. (21) into Eq. (19), one can reexpress the coupling $\mathcal{H}'$ in the Bogoliubov quasiparticle basis that diagonalizes the $\mathcal{H}_0$ term [see Eq. (9)], obtaining

$$\begin{aligned}\mathcal{H}' = -\frac{\mathrm{e} v_F}{2} A(t) \sum_{0 \leqslant E_i, E_j < \Delta_0} &(g_{ij}\gamma_i^\dagger \gamma_j - g_{ij}^* \gamma_i \gamma_j^\dagger \\ &+ \tilde{g}_{ij}\gamma_i^\dagger \gamma_j^\dagger + \tilde{g}_{ji}^* \gamma_i \gamma_j),\end{aligned} \tag{22}$$

where

$$g_{ij} = \int dx (\Phi_i^{(+)}(x))^\dagger (\tau_0 \otimes \sigma_z) \Phi_j^{(+)}(x) \tag{23}$$

and

$$\tilde{g}_{ij} = \int dx (\Phi_i^{(+)}(x))^\dagger ((-i\tau_y) \otimes \sigma_x)(\Phi_j^{(+)}(x))^* \tag{24}$$

are dimensionless overlap integrals. The g_{ij} coefficients in Eq. (23), which by definition are bounded ($|g_{ij}| \leqslant 1$) and fulfill the property $g_{ji} = g_{ij}^*$, identify the matrix entries of the current density operator (19), divided by ev_F, between ABSs. In particular, a diagonal entry g_{ii} is related to the spatially averaged current carried by the ith ABS, while the off-diagonal entries g_{ij} (with $i \neq j$) describe the processes of photoexcitation from the jth ABS to the ith ABS. Notably, despite the expression (19) of the QSHI edge state current density is independent of the momentum p_x and is therefore quite different from the case of conventional materials with a parabolic spectrum such as nanowires, one can show that the off-diagonal entries g_{ij} (with $i \neq j$) are related to the electric dipole operator, which in Nambu formalism acquires the form $d = e\,x\,(\tau_z \otimes \sigma_0)/2$. To this purpose, it is sufficient to realize that the major contribution to the g_{ij} coefficients stems from the weak link region where the ABSs are localized. Inside the weak link, one has $[H_{\rm BdG}(x), d] = -ie\hbar v_F(\tau_0 \otimes \sigma_z)/2 = -i\hbar J$. Applying the ABS wavefunctions $\Phi_i^\dagger$ (on the left) and Φ_j (on the right) of this relation and exploiting $H_{\rm BdG}\Phi_i = E_i\Phi_i$, one finds

$$\Phi_i^\dagger(\tau_0 \otimes \sigma_z)\,\Phi_j = \frac{2i(E_i - E_j)}{e\hbar v_F}\Phi_i^\dagger\, d\;\Phi_j. \tag{25}$$

For this reason, the ASQ spin-flip processes determined by g_{ij} are electric dipole-induced spin processes.

As far as $\tilde{g}_{ij}$ are concerned, they are also bounded ($|\tilde{g}_{ij}| \leqslant 1$), fulfill $\tilde{g}_{ji} = -\tilde{g}_{ij}$, and represent the matrix entries of Eq. (19) between the charge conjugated of the jth ABS and the ith ABS. The $\tilde{g}_{ij}$ physically describe photoexcitation from the superconducting condensate to a pair (i, j) of ABSs, as can be deduced from inspection of Eq. (22).

A. Single-particle density matrix in Nambu formalism

The quantum state of the ASQ can be characterized by the $2N \times 2N$ single-particle density matrix in Nambu formalism

$$\boldsymbol{\rho} = \langle \boldsymbol{\Gamma}^\dagger \otimes \boldsymbol{\Gamma}\rangle = \begin{pmatrix} \rho^{ee} & \rho^{eh} \\ \rho^{he} & \rho^{hh} \end{pmatrix}, \tag{26}$$

where the entries of the diagonal particle and hole blocks are

$$\rho_{ij}^{ee} = \langle \gamma_j^\dagger \gamma_i\rangle, \quad \rho_{ij}^{hh} = \langle \gamma_j \gamma_i^\dagger\rangle, \tag{27}$$

while for the anomalous off-diagonal blocks one has

$$\rho_{ij}^{eh} = \langle \gamma_j \gamma_i\rangle, \quad \rho_{ij}^{he} = \langle \gamma_j^\dagger \gamma_i^\dagger\rangle, \tag{28}$$

with $i, j = 1, \ldots, N$ (number of ABSs). The fermionic nature of the operators γ_i's implies that $\rho_{ii}^{eh} = \rho_{ii}^{he} = 0$.

It is possible to show that the single-particle density matrix defined in Eq. (26) fulfills a Liouville–von Neumann equation governed by the BdG Hamiltonian in the γ-Bogoliubov quasiparticle basis. Explicitly, in the interaction (I) picture, one has

$$i\hbar\frac{d\boldsymbol{\rho}_{\rm I}}{dt} = [H_{\rm I}'(t),\ \boldsymbol{\rho}_{\rm I}(t)], \tag{29}$$

where

$$H_{\rm I}'(t) = -ev_F A(t)\begin{pmatrix} \mathsf{g}_{\rm I}^{ee}(t) & \tilde{\mathsf{g}}_{\rm I}^{eh}(t) \\ \tilde{\mathsf{g}}_{\rm I}^{he}(t) & \mathsf{g}_{\rm I}^{hh}(t) \end{pmatrix} \tag{30}$$

is the perturbing Hamiltonian, with

$$\left(\mathsf{g}_{\rm I}^{ee}(t)\right)_{ij} = g_{ij}\, e^{i\frac{(E_i - E_j)t}{\hbar}}, \tag{31}$$

$$\left(\mathsf{g}_{\rm I}^{hh}(t)\right)_{ij} = -g_{ij}^*\, e^{-i\frac{(E_i - E_j)t}{\hbar}}, \tag{32}$$

$$\left(\tilde{\mathsf{g}}_{\rm I}^{eh}(t)\right)_{ij} = \tilde{g}_{ij}\, e^{i\frac{(E_i + E_j)t}{\hbar}}, \tag{33}$$

$$\left(\tilde{\mathsf{g}}_{\rm I}^{he}(t)\right)_{ij} = \tilde{g}_{ji}^*\, e^{-i\frac{(E_i + E_j)t}{\hbar}}. \tag{34}$$

Here, g_{ij} and $\tilde{g}_{ij}$ are given by Eqs. (23) and (24), respectively, while the time-dependent phase factors are related to the ABS energy levels E_i's characterizing the $2N \times 2N$ unperturbed Hamiltonian

$$H_0 = \begin{pmatrix} H_0^{ee} & 0 \\ 0 & H_0^{hh} \end{pmatrix}, \tag{35}$$

which is by definition block diagonal with particle and hole blocks given by

$$H_0^{ee} = \begin{pmatrix} E_1 & 0 & \ldots \\ 0 & E_2 & \ldots \\ 0 & 0 & \ddots \end{pmatrix}, \quad H_0^{hh} = -H_0^{ee}. \tag{36}$$

B. Electric dipole transition amplitudes

The structure of the radiation coupling term (30) shows that the diagonal coefficients g_{ii} lead to a renormalization of the unperturbed ABS eigenvalues in Eq. (36), which *a priori* could affect the resonance frequency for the inter-ABS transitions. Moreover, the $\tilde{g}_{ij}$ coefficients couple the electron-hole sectors in Eq. (30). Although our simulations to be presented in the next section fully take into account the g_{ii} and $\tilde{g}_{ij}$ coefficients too, we anticipate that both these effects turn out to be negligible, at least in the prototypical case of a JJ hosting two ABSs, as we shall discuss at the end of Sec. IV. The key ingredient to induce the spin-flip transitions and to enable the ASQ manipulation is the *off-diagonal* coefficients g_{ij} (with $i \neq j$), i.e., the electric dipole transition entries, which we would like to discuss here.

For definiteness, we focus on the case of a JJ characterized by two ABSs, obtained by setting the weak link length parameter to $\lambda = 2$ [see Eq. (14)]. By considering the presence of a magnetic disorder barrier Eq. (15) with energy height $m_\perp$ and length L_m inside the weak link ($0 \leqslant L_m \leqslant L$), we have investigated how the electric dipole transition amplitude g_{12} between the two ABSs depends on the various parameters of the barrier and the junction. Figure 4 analyzes the dependence of g_{12} on the spatial extension L_m of the barrier, for a fixed value of the barrier "area" parameter $\alpha = L_m m_\perp/\hbar v_F$. Solid curves illustrate the behavior for a vanishing chemical potential $\mu = 0$ and show that g_{12} is roughly independent of the spatial extension L_m of the barrier. The various curves refer to different values of the superconducting phase difference ϕ. In particular, one has $|g_{12}| \lesssim 1$ for vanishing phase difference ($\phi = 0$), while $|g_{12}|$ decreases with increasing ϕ and reaches its minimal value for $\phi = \pi$. The dashed curves describe the case $\mu = \Delta_0/2$. As one can see, a finite value $|\mu| < \Delta_0$ of the chemical potential leads to a slight reduction of g_{12} only for $L_m \sim L$, whereas g_{12} is independent of the value of μ for

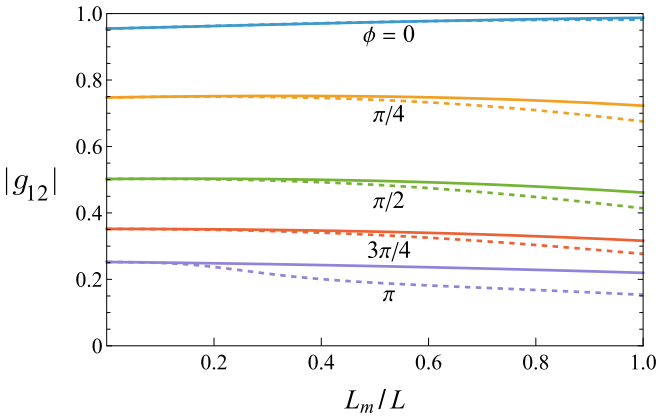

FIG. 4. The magnitude $|g_{12}|$ of the electric-dipole transition amplitude between two ABSs is shown as a function of the ratio of the spatial extension L_m of the magnetic disorder to the JJ weak link length L, for a fixed value of the magnetic barrier parameter $\alpha = m_\perp L_m/\hbar v_F = 0.5$, and for different values of the superconducting phase difference ϕ. Solid curves refer to chemical potential $\mu = 0$, while dashed curves to $\mu = \Delta_0/2$. The magnetic disorder is distributed around the center $x_0 = 0$ of the weak link, which has a length parameter $\lambda = 2$.

$L_m \ll L$. Notice also that such a reduction depends on ϕ as well, with the curves at $\phi = 0$ being insensitive to the variations of μ. In fact, it can be shown that only far away from the Dirac point $|\mu| \gg \Delta_0$ and for phase differences $\pi/2 < \phi \lesssim \pi$, the dependence of g_{12} on L_m/L becomes significant. These results suggest that, operating sufficiently close to the Dirac point ($|\mu| < \Delta_0$), a single δ-like impurity and a uniformly distributed barrier with equal barrier "area" $\alpha \lesssim 1$ yield a quite similar electric dipole transition amplitude.

For this reason, we now focus on the case of a magnetic δ impurity, whose transmission coefficient acquires a simple expression $T_E = T_\delta = 1/\cosh^2\alpha$ that is independent of the energy and of the chemical potential μ. Figure 5 displays $|g_{12}|$ as a function of the transmission coefficient T_δ, for various values of the impurity position within the weak link, for a superconducting phase difference $\phi = \pi/2$. Two features are noteworthy. First, in the limit $T_\delta \to 1$, one can see that $|g_{12}| \to 0$ for all curves. Indeed in this limit, which corresponds to the absence of disorder, the two ABSs become spin-z eigenstates with two different eigenvalues, which have therefore vanishing matrix entries of the current. This shows the crucial role played by the magnetic doping in enabling the ASQ manipulation. Second, the electric dipole transition amplitude is quite sensitive to the introduction of magnetic doping, since g_{12} exhibits a steep increase even for a small reduction of transmission T_δ from 1. Thus, the transition amplitude is a non-negligible fraction of 1, even for a relatively weak impurity, i.e., for a transmission as high as 90%.

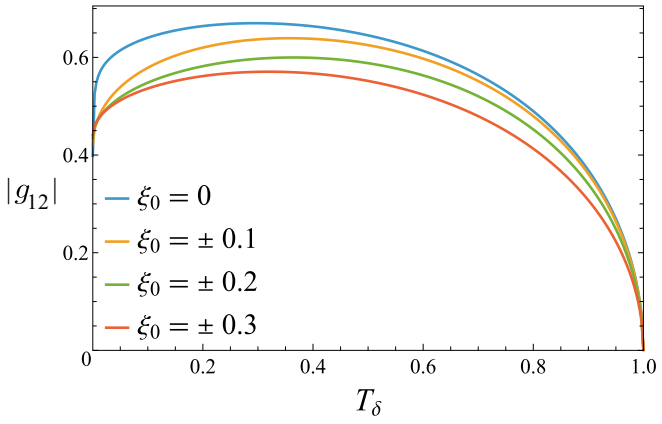

FIG. 5. The magnitude $|g_{12}|$ of the electric dipole transition amplitude between two ABSs is shown as a function of the transmission T_δ of a magnetic δ impurity present in the weak link, for different values of the impurity relative location $\xi_0 = x_0/L$ from the weak link center. The length parameter is $\lambda = 2$, and the superconducting phase difference is $\phi = \pi/2$.

IV. MANIPULATION OF THE ASQ

In this section, we demonstrate the possibility of realizing quantum logic gates on the QSHI-based ASQ by applying a properly tailored electromagnetic pulse. To this aim, we present a few prototypical simulated experiments, performed by a fixed-time-step solution of the Liouville–von Neumann equation (29), where we have considered an electromagnetic excitation consisting of a sequence of independent Gaussian pulses, each pulse being described by the vector potential

$$A(t) = \frac{\mathcal{E}_0}{\omega} G(t) \cos[\omega(t - \bar{t}) + \varphi]. \tag{37}$$

Here, $\mathcal{E}_0$ denotes the magnitude of the electric field, ω the pulse frequency, and φ a phase, whereas

$$G(t) = \exp\left[-\frac{(t - \bar{t})^2}{2\tau^2}\right] \tag{38}$$

is a Gaussian time envelope profile, centered around the time $\bar{t}$ and with a duration parameter τ (see, e.g., the violet curve in Fig. 6). Moreover, we shall consider the adiabatic excitation regime, i.e., $\omega\tau \gg 1$, where the Gaussian envelope of each pulse contains a large number of oscillations, and the electric field corresponding to the vector potential in Eq. (37) is well approximated by a Gaussian pulse as well

$$E(t) \simeq \mathcal{E}_0 G(t) \sin[\omega(t - \bar{t}) + \varphi]. \tag{39}$$

For definiteness, we consider a helical JJ realized with a HgTe/CdTe QSHI proximized by Nb films. The Fermi velocity of the helical edge states is taken as $v_F = 5 \times 10^5$ m/s [29], and the induced superconducting pairing is assumed to be $\Delta_0 = 1$ meV. As an ASQ architecture, we start by considering a helical JJ with two ABSs, obtained by taking the parameter $\lambda = 2$, corresponding to a weak link length $L \simeq 660$ nm [see in Eq. (14)]. Moreover, we focus on the regime of a localized magnetic impurity, where the ABSs are depicted by the red dashed curve of Fig. 2. We have considered a Gaussian pulse with a frequency $\omega = (E_2 - E_1)/\hbar$ resonant with the ASQ, applied for a pulse duration $\tau = 80$ ps, around a time $\bar{t} = 250$ ps. We suppose that the ASQ can be prepared in the computational input states $|0\rangle$ or $|1\rangle$. The former corresponds to a full occupation of the lower ABS ($f_1 = \rho_{11}^{ee} = 1$) and an empty upper ABS ($f_2 = \rho_{22}^{ee} = 0$), the latter to the opposite situation ($f_1 = 0$, $f_2 = 1$), respectively.

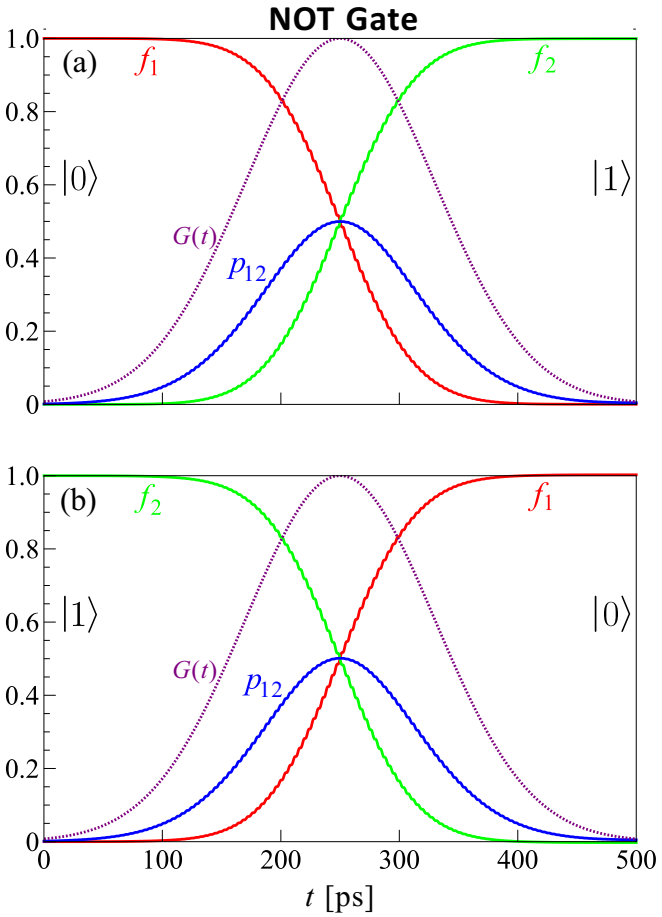

FIG. 6. Simulation of the implementation of a NOT gate in the QSHI-based ASQ. A magnetic δ impurity characterized by transmission coefficient $T_\delta = 0.8$ is located at position $x_0 = L/4$ inside the JJ weak link. The length parameter is $\lambda = 2$, and the superconducting phase difference is $\phi = \pi/2$.

A quantum logic gate transforms the input states $|0\rangle$ or $|1\rangle$ into specific output states by performing an appropriate rotation by an angle θ in the computational basis space. Two noteworthy aspects are relevant to describe its realization. First, the product $\mathcal{E}_0\,\tau$ of the amplitude and the duration of the pulse must be suitably calibrated to perform an on-demand rotation. For a two-level system characterized by an electric dipole transition amplitude g_{12}, the suitable value of $\mathcal{E}_0\tau$ can be given the analytical expression [81]

$$\mathcal{E}_0\tau = \frac{(E_2 - E_1)\,\theta}{\sqrt{2\pi}\,\mathrm{e}v_F|g_{12}|}, \tag{40}$$

provided off-resonant coupling terms are neglected. The second aspect to be emphasized is that, *a priori*, the conditions to manipulate the ASQ depend on the superconducting phase difference ϕ in a nontrivial way. Indeed, on the one hand, in order to maximize the interlevel energy splitting $E_2 - E_1$, it is advisable to operate at $\phi \neq 0$, preferably near $\phi \sim \pi$, as shown in Fig. 2. On the other hand, the electric dipole transition amplitude $|g_{12}|$ is minimal at such ϕ value, and maximal at $\phi = 0$, as shown in Fig. 4. Moreover, while for $\phi = 0$ the diagonal matrix elements g_{11} and g_{22} are absent, they become significantly different from zero for increasing values of ϕ, giving rise to energy renormalization effects during the ASQ manipulation. We have performed our simulations at the trade-off value of $\phi = \pi/2$, yielding $E_2 - E_1 \simeq 0.52$ meV, and $|g_{12}| \simeq 0.43$. However, as we shall discuss below, the results do not change significantly with other values of superconducting phase difference.

We start by describing the simulation of the quantum NOT gate, which corresponds to a rotation by $\theta = \pi$ and converts $|0\rangle \to |1\rangle$ and $|1\rangle \to |0\rangle$. The dynamical simulation is shown in Fig. 6. Specifically, panel (a) shows the continuous transition of the $|0\rangle$ input state into the $|1\rangle$ output state at the end of the pulse, while panel (b) shows the reversed process $|1\rangle \to |0\rangle$. The red and green curves display the dynamical evolution of the ABS populations f_1 and f_2, respectively. The dotted magenta curve illustrates the time profile characterizing the applied pulse and described by the Gaussian function $G(t)$ in Eq. (38). Along with the change in the ABS populations, a nonvanishing value of the interlevel polarization emerges during the two excitation processes. Indeed, the blue curves in Fig. 6 illustrate the evolution of its absolute value $p_{12} = |\rho^{ee}_{12}|$. As one can see, while p_{12} is always vanishing before and after the pulse, it reaches a maximum value of $1/2$ exactly at the center of the Gaussian pulse, where also the two populations reach the very same value ($f_1 = f_2 = 1/2$), as dictated by the unitary dynamical evolution.

Let us now turn to the Hadamard gate, which plays a central role in many quantum information processing protocols [82]. It corresponds to a rotation by an angle $\theta = \pi/2$ and operates as follows:

$$|0\rangle \to \frac{1}{\sqrt{2}}(|0\rangle + |1\rangle), \tag{41}$$

$$|1\rangle \to \frac{1}{\sqrt{2}}(|0\rangle - |1\rangle), \tag{42}$$

i.e., converting the ASQ input states into the equally weighted quantum superpositions, characterized by $f_1 = f_2 = 1/2$ and by $\rho^{ee}_{12} = \rho^{ee}_{21} = \pm 1/2$, respectively. Its dynamical implementation is illustrated in Fig. 7, where the two panels (a) and (b) describe the processes [Eqs. (41) and (42)], respectively. Note that the corresponding population and polarization time profiles confirm that the ASQ state after the Hadamard gate processing is equivalent to the ASQ state in the middle of a NOT gate (see Fig. 6).

Although the above results have been obtained for the trade-off value $\phi = \pi/2$ of the superconducting phase difference, we have verified that the value of ϕ has in fact a negligible impact on the quality of the quantum manipulation. For instance, at $\phi = 0$, the simulated experiments lead to results that are quite similar to the ones shown in Figs. 6 and 7, in spite of differences in the corresponding values of interlevel energy splitting ($E_2 - E_1 \simeq 0.25$ meV) and transition amplitude ($|g_{12}| \simeq 0.94$). The only minor feature that emerges for $\phi \neq \pi/2$ is the appearance of small and wiggly modulations of the two populations and of the interlevel polarization. The period of such small modulations corresponds to a frequency 2ω and is due to the off-resonant contributions that, while being often neglected in models based on the rotating-wave approximation, are fully taken into account by our approach. Apart from such a minor feature, the robustness of the result to

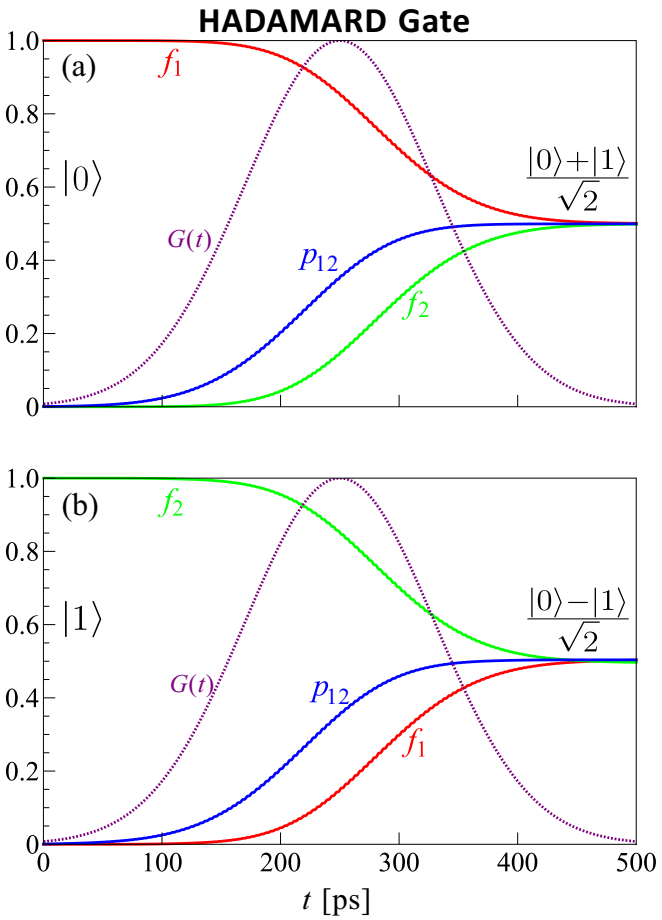

FIG. 7. Simulation of the Hadamard gate. The parameters are the same as in Fig. 6.

the choice of ϕ proves the accuracy of the simulated quantum gates. In turn, this also shows that the presence of nonzero diagonal matrix elements g_{11} and g_{22} does not significantly affect the simulated experiments of Figs. 6 and 7. This can be explained by observing that, in the envisaged adiabatic-excitation regime $\omega\tau \gg 1$, the Gaussian pulses contain a large number of oscillations, and therefore the energy renormalization effects mentioned in Sec. III effectively average out to zero.

Finally, a comment is in order about the off-diagonal blocks $\tilde{\mathrm{g}}_{\mathrm{I}}^{eh}(t)$ and $\tilde{\mathrm{g}}_{\mathrm{I}}^{he}(t)$ in Eq. (30), which physically describe the simultaneous photoexcitation of two electrons from the superconducting condensate to the generic pair of ABS i and j. In all the simulated experiments presented so far, which refer to the case of a JJ with two ABSs ($N = 2$) and involve an initial state with $f_1 + f_2 = 1$, the matrix entries $\tilde{g}_{ij}$ do not contribute at all to the time evolution of the density matrix, as can also be proven by a few algebra steps. However, as we shall discuss in the next section, the $\tilde{g}_{ij}$ coefficients may play a crucial role when more ABSs are present.

V. DISCUSSION

This section is devoted to discuss some aspects concerning the implementation in realistic systems, the preparation of the initial quantum state, and the dissipation and decoherence effects.

A. Possible experimental implementations

The QSHI state has been experimentally observed in HgTe/CdTe [32–35] quantum wells, in InAs/GaSb [36,37] bilayers, in Bi bilayers [38–40], as well as in WTe_2 monolayers [41–43]. QSHI-based JJ have been realized using various superconductors. In particular, Al contacts have been used in InAs/GaSb implementations [51], $NbSe_2$ contacts in WTe_2 monolayers [83], while HgTe has been proximized with Nb films [52,55], Al contacts [50,53], and MoRe electrodes [54]. Moreover, magnetic doping of QSHI has been recently achieved with ferromagnetic Fe impurities deposited on Bi bilayers [60], and with dilute Mn atoms in HgTe-based implementations [54,61].

The simulations we have presented are inspired to a HgTe/CdTe-based QSHI proximized by Nb contacts, which seems to be most promising platform for the ASQ realizations, since decoherence effects due to inelastic scattering mechanisms are expected to be reduced, as we shall argue below in Sec. V C. Moreover, experimental evidence shows that in HgTe/CdTe quantum wells edge channels carry significantly more current than what one could expect in a nontopological conductor [35,50], ruling out possible edge conduction of topologically trivial origin arising from unwanted edge doping during fabrication or from band bending.

Three more aspects concerning the experimental implementations deserve a comment. First, in setups of proximized QSHI, the superconducting films typically cover both edges of the QSHI bar. However, because the two edges are usually separated by a distance W of several micrometers, i.e., longer than the superconducting phase coherence length [50,54], the two weak links can be considered as independent. Thus, our model, where only one edge has been considered, reliably applies. A second comment is about the possible leakage of quasiparticles into the weak link (quasiparticle poisoning [84,85]). In QSHI-based JJ, it has been predicted that quasiparticle poisoning might induce a change in the Josephson current periodicity when the superconducting phase ϕ varied [77–79]. In an ASQ, however, one customarily operates around a fixed value of ϕ, which sets the energy separation of the ASQ states and the radiation frequency to be used for the manipulation. Still, quasiparticle poisoning should be limited experimentally, as it may alter the ABS occupancy. Poisoning by quasiparticles originating from the superconductors can be reduced by modulating the thicknesses of the superconducting films, thereby trapping quasiparticles sufficiently far away from the weak link [19]. Other sources of quasiparticle poisoning can be ascribed to an additional localized level present inside the weak link, which could effectively act as a quasiparticle "bath" for the ASQ, as has been observed in nanowire setups [19]. However, while in nanowires such bound states could emerge from a local confinement due to spin-orbit inhomogeneities, this possibility is reduced for the helical states of a QSHI, whose linear and helical spectrum hinders confinement. For these reasons, we expect that in the proposed setup the quasiparticle poisoning effect can be mitigated, at least as much as can be done in current nanowire-based ASQ

implementations. The third aspect to be mentioned is that, different from conventional materials, the zero-energy crossing of the ABS spectrum at $\phi = \pi$ shown in Fig. 2 is robust. Indeed, due to the helical nature of the topological states, the number of degrees of freedom in a QSHI-based JJ is halved as compared to conventional JJ, and the ABS are nondegenerate fermionic states. As a consequence, the two energy levels $\pm E_1(\phi)$ crossing at zero energy at $\phi = \pi$ shown in Fig. 2 are related to two fermion parity sectors ($\gamma_1^\dagger \gamma_1 = 0, 1$, i.e., even/odd) of the excitation Hamiltonian $\mathcal{H}_1 = E_1(\phi)(\gamma_1^\dagger \gamma_1 - 1/2)$ [76,77]. As a consequence, the zero-energy crossing is topologically protected [75,76] and cannot even be removed by quasiparticle poisoning that switches the parity.

Finally, it is worth mentioning that the weak link of the JJ is typically embedded in a superconducting loop, which controls the superconducting phase difference through an external flux. In turn, the loop is also inductively coupled to a microwave resonator, usually an LC circuit, whose frequency depends on the occupancy of the ABSs. The manipulation of the ASQ can be induced either by applying an ac signal through a gate (all-electric control) or by modulating the magnetic flux through an ac in a conductor coupled to the superconducting loop [8–19]. On the one hand, an all-electric control of the ASQ offers great advantages in terms of scalability, integration with classical control circuits on-chip, and overall simplicity in the setup structure. On the other hand, the timescale of electrical manipulation is the nanosecond, which may limit the number of operations that can be performed within the ASQ decoherence time. A possible alternative strategy could be an optical control performed with laser pulses. While this integrated technology is certainly more complex from the viewpoint of the setup architecture, in the case of spin qubits realized with semiconductor quantum dots, it was proven to enable the control in the picosecond or even femtosecond timescales, thereby increasing by orders of magnitude the number of operations that can be performed within the decoherence time [6,86–88].

B. Preparation of the initial state

In Sec. IV, we have presented a few simulations of quantum information processing assuming that the ASQ can be prepared in an input state $|0\rangle$ or $|1\rangle$. Since in the low-temperature limit the equilibrium population of all the ABSs vanishes, it is crucial to identify a reliable protocol for the preparation of the initial computational state. As an illustrative example, let us discuss for instance the preparation of the $|0\rangle$ state, characterized by an energy E_1. The physical protocol that we aim to mimic, inspired by Ref. [1], consists in photoexciting the condensate with a frequency $\Delta_0 + E_1 < \hbar\omega < 2\Delta_0$. In this way, one quasiparticle is excited in the state with E_1, while the other one is promoted to the continuum spectrum and plays no further role for the ASQ, for it leaves the weak link within a timescale of the order $\tau_e \sim L/v_F$. In order to simulate this protocol, in principle one would need to include, together with the two discrete ABS of the ASQ, also a huge number of closely spaced states with energies $E > \Delta_0$ describing the continuum. However, as far as the simulation of the initial state preparation is concerned, for practical computational purposes nothing changes to the ASQ

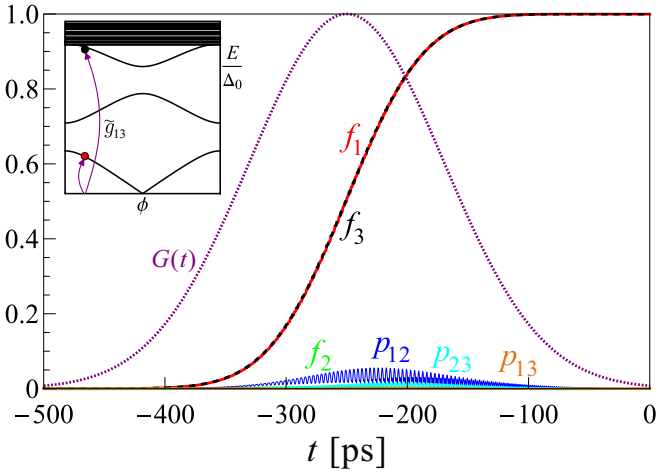

FIG. 8. Simulation of the initial state preparation (negative times) induced by an electromagnetic pulse with $\bar{t} = -250$ ps and $\tau = 80$ ps. The preparation protocol is based on a JJ with three ABSs, and a two-quasi-particle photoexcitation from the condensate (see text), as depicted in the inset. The parameters of the weak link are $\lambda = 3$ and $\phi = \pi/4$, while the magnetic δ impurity, located at position $x_0 = L/4$ from the center of the weak link, has a transmission coefficient $T_\delta = 0.8$.

preparation process if one considers a third discrete level, with an energy E_3 lower but very close to Δ_0 (see inset of Fig. 8), that effectively plays the role of the continuum. This enables one to mimic the role of the continuum spectrum, while retaining a limited number of states in the simulation. Thus, starting from the low-temperature equilibrium state ($f_1 = f_2 = f_3 = 0$), one could fully promote two electrons from the superconducting condensate to the lowest energy level E_1 and to the highest energy level E_3. This type of process relies on the $\tilde{g}_{13}$ coefficient and can be easily induced via a properly tailored electromagnetic pulse with frequency $\omega = (E_1 + E_3)/\hbar$. Indeed, if the intermediate energy level E_2 is sufficiently separated from both level E_1 and level E_3, the excitation pulse will not change its low-temperature equilibrium population ($f_2 = 0$). As a result of such preliminary photoexcitation process, the three-level weak link is then promoted into the physical state $f_1 = 1$, $f_2 = 0$, and $f_3 = 1$, as sketched in the inset of Fig. 8, and therefore the ASQ is correctly prepared in its computational state $|0\rangle$ ($f_1 = 1$ and $f_2 = 0$).

The two requirements of (1) ABS energy levels relatively far from each other and (2) an electric dipole transition amplitude $\tilde{g}_{13}$ significantly different from zero are fulfilled by choosing a superconducting phase difference $\phi = \pi/4$ in the three-ABS weak link described in the inset of Fig. 8. Indeed, in this case one has $E_1 \simeq 0.25$ meV, $E_2 \simeq 0.51$ meV, and $E_3 \simeq 0.98$ meV, as well as $|g_{12}| \simeq 0.67$ and $|\tilde{g}_{13}| \simeq 0.10$, which corresponds to an electron-pair generation energy $E_1 + E_3 \simeq 1.24$ meV and to an ASQ energy splitting $E_2 - E_1 \simeq 0.26$ meV. The result of simulated experiments preparing the initial state $|0\rangle$ is shown in the negative time axis of Fig. 8, where the electron-pair photoexcitation described above is realized via a properly tailored Gaussian pulse centered around the time $\bar{t} = -250$ ps and with a pulse duration of 80 ps.

The accuracy of our simulated experiment fully confirms the reliability of the proposed computational-state preparation.

C. Energy dissipation and decoherence phenomena

As is well known [89–93], a major limitation of solid-state quantum information processing platforms is the presence of energy dissipation and decoherence (DD) phenomena. Although helical states are topologically protected from elastic backscattering off time-reversal symmetric perturbations, dissipation and decoherence can arise from inelastic processes. Here, we would like to analyze first the various possible sources of these effects in the proposed ASQ, and then provide an estimate of these effects in a worst case scenario.

1. Inelastic scattering mechanisms

Hyperfine interaction. We start with the hyperfine interaction, which couples electron and nuclear spins, and is considered the main origin of the relatively short decoherence time in the current ASQ implementations with InAs nanowires [14,15,18–20]. In QSHI realized with InAs/GaSb bilayers [36,37], the hyperfine constant is of the same order of magnitude as nanowires [48,49,94]. However, in HgTe/CdTe, due to the limited percentage of crystal atoms with a nonvanishing nuclear spin (at most 17%) and a smaller nuclear spin, the hyperfine coupling constant is smaller by more than one order of magnitude [46,47,49]. By Fermi golden rule, one can therefore expect that spin relaxation times due to nuclear spin coupling are enhanced by roughly two orders of magnitude.

Electron-phonon coupling. Another possible inelastic scattering is the coupling to phonons. Although acoustic phonons do not couple to the spin degree of freedom directly, their interplay with Rashba impurities present in the QSHI might in principle break the topological protection of the edge states. However, this effect is known to have a quite negligible impact on the normal current through the helical edge state, at least to leading order in the Rashba disorder strength [44,45]. We expect that a similar situation occurs when the helical states are proximized by superconductors, and that phonon-induced dynamical spin-flip processes are not significant.

Electron-electron interaction. As is well known, since in an ASQ charge can fluctuate back and forth from the JJ weak link to the superconductors through Andreev reflections, Coulomb charging energy effects are strongly suppressed with respect to conventional quantum dots. Yet, in the ASQ proposed here, where the edge states of the QSHI are one-dimensional, electron-electron interaction can give rise to collective excitations, realizing a helical Luttinger liquid, characterized by a parameter $K \leqslant 1$ that identifies the strength of the repulsive screened Coulomb interaction (with $K = 1$ describing the non-interacting case). Spin decoherence caused by two-particle backscattering with spin-flip processes can only occur at commensurate filling values (Umklapp processes), and is relevant only for $K < 1/2$, i.e., for relatively strong interaction [65]. However, interaction can also interplay with magnetic impurities [45]. In the case of static impurities considered here, single-particle backscattering with spin flip is relevant for $K < 1$, thereby enhancing the ABS spin texture modification, but with no impact on decoherence. In the presence of dynamical quantum impurities, such as Kondo impurities, the scenario depends on the interaction strength, on the possible impurity anisotropy, and on the temperature regime [61,65–70]. However, at temperatures below the Kondo temperature, two-particle backscattering causing spin decoherence is relevant only for very strong interaction ($K < 1/4$).

Thus, the decoherence effects heavily depend on the actual value of the interaction strength K. Although experimental measurements of K are quite limited [95], various theoretical studies have estimated that in QSHI realized with InAs/GaSb quantum wells the interaction is relatively strong ($K \simeq 0.4$), while in HgTe/CdTe-based QSHI it is quite weak $K \lesssim 1$ [66,96–98]. Moreover, in the ASQ setup proposed here (see Fig. 1), where the helical Luttinger liquid is proximized by superconductors, further aspects are noteworthy.

On the one hand, the problem of a Luttinger liquid contacted to superconductors is computationally nontrivial, and analytical approaches are only viable in the case of tunnel contacts [99,100] or in the regime of a very long junction $L \gg \xi_S$ [101]. On the other hand, the presence of two superconducting films deposited on the QSHI is expected to entail two effects. First, an enhancement of the screening effects, thereby leading to a reduction of the effective electron-electron interaction and the related decoherence effects. Second, the finite length L of the weak link "cuts" the renormalization group flow at a finite Thouless energy scale $E_L = \hbar v_F/L$. Thus, at given values of interaction strength K and weak link length L characterizing a specific setup, the results obtained for the noninteracting case are expected to be quantitatively but not qualitatively modified by the interaction. This expectation is confirmed, for instance, by the results known in the case of a strong magnetic impurity present inside a very long helical JJ, where the critical current has been shown to behave as $I_c \propto E_L^{4/K}$ [78]. A similar modification occurs in the present case of an intermediate length junction, where the matrix entries g_{ij} of the current operator (19) are expected to depend in a K-dependent manner on an energy scale that is a combination of the E_L and Δ_0. In HgTe/CdTe quantum wells, where $K \simeq 1$, the modifications with respect to the noninteracting case $K = 1$ are expected to be negligible.

2. Simulation of dissipation and decoherence effects in the worst case scenario

A thorough analysis taking into account microscopically all the above inelastic scattering mechanisms leading to DD processes in the proposed ASQ implementation is out of the scope of the present paper. Yet, we would like to provide some quantitative information about the impact of these effects. As argued above, there are various motivations to expect that dissipation and decoherence effects in JJ based on QSHI should be suppressed as compared to current nanowire implementations, particularly in the case of HgTe quantum wells proximized by Nb films, and our simulations in Sec. IV were inspired by such setup. Moreover, a quality factor of a quantum hardware is the ratio of the decoherence time to the typical operational timescale, rather than the decoherence time as an absolute time.

Thus, we have considered the "worst case scenario" where the decoherence time in the proposed QSHI-based ASQ is similar to the one of the current nanowire implementations,

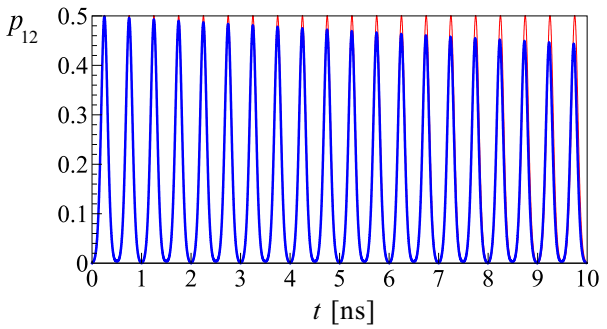

FIG. 9. Simulation of a sequence of operations (20 NOT gates): Time evolution of the polarization p_{12}. The thin red line describes the case of a unitary evolution, while the blue thick curve describes the behavior in the presence of dissipation and decoherence phenomena, accounted for via the phenomenological model in Eq. (43) choosing $T_1 = 100$ ns and $T_2 = 50$ ns (see text). The JJ parameters are the same as in Fig. 6.

and we have tested how many operations one could perform within such a timescale. To this purpose, we have adopted a generalized phenomenological T_1-T_2 model [90,93], where T_1 and T_2 are the relaxation and decoherence timescales, respectively. Specifically, while the simulated experiments presented in Sec. IV result from a fully coherent dynamics, here we have included DD effects by adding to each of the four blocks of the Nambu density matrix $\boldsymbol{\rho}$ the following incoherent time evolution term:

$$\left.\frac{d\rho_{ij}^{\alpha\beta}}{dt}\right|_{\text{inc}} = -\Gamma_{ij}\left(\rho_{ij}^{\alpha\beta} - (\rho_{\text{eq}})_{ij}^{\alpha\beta}\right), \tag{43}$$

with

$$\Gamma_{ij} = \frac{\delta_{ij}}{T_1} + \frac{1-\delta_{ij}}{T_2}, \tag{44}$$

where $\alpha, \beta = e, h$ and ρ_{eq} denotes the (diagonal) equilibrium density matrix. The diagonal terms ($i = j$) relax to their equilibrium values within the energy-dissipation time T_1, while the off-diagonal terms ($i \neq j$) decay to zero within the decoherence time T_2. It is important to stress that, in order to preserve the positive-definite character of the density matrix, it is necessary to choose $T_1 \geqslant 2T_2$ [81].

The simulated experiment presented in Fig. 9 corresponds to a sequence of 20 NOT gates and shows the time evolution of the interlevel polarization p_{12}, which is characterized by a sequence of maxima, one for each NOT gate (see Fig. 6). In particular, the thin red curve refers to the unitary evolution, while the blue thick curve describes the case where DD phenomena are accounted for via the phenomenological model in Eq. (43). The decoherence time has been chosen as $T_2 =$ 50 ns, i.e., in agreement with the value characterizing current ASQ implementations with nanowires [8,14,15,17,19], while the relaxation time has been set to $T_1 = 100$ ns, i.e., the minimal compatible with the constraint $T_1 \geqslant 2T_2$ mentioned above. Here, the system as well as the simulation parameters are the same as in Fig. 6. While in the fully coherent case (red curve) p_{12} exhibits a periodic behavior, where all the polarization maxima reach the very same value ($p_{12} = 1/2$), in the presence of DD phenomena (blue curve) a small decrease of the polarization maxima occurs, which is on the order of 10% at the end of the simulation (10 ns), consistently with the decoherence time $T_2 = 50$ ns used in the simulation. Our analysis shows that even in the worst case scenario, where the decoherence time is the same as in the current nanowire realizations, incoherent processes have a negligible impact on the realization of the quantum gates based on the QSHI-JJ. Indeed, the proposed ASQ manipulation allows one to realize tens of quantum operations within the selected DD times.

VI. CONCLUSIONS

We have proposed an implementation of ASQs based on a JJ realized with the helical edge states of a QSHI, proximized by two superconducting films, as illustrated in Fig. 1. We have shown that the presence of magnetic doping alters the natural spin texture of the ABSs and leads to nonvanishing electric dipole transition amplitudes (see Figs. 4 and 5), enabling the possibility to manipulate the ASQ with a radiation, without the need for an externally applied Zeeman field, and without invoking ancillary qubits. As illustrative examples, we have simulated the realization of NOT and Hadamard quantum gates by suitably tailored electromagnetic pulses applied to the QSHI-JJ, as shown in Figs. 6 and 7, respectively. A possible strategy to prepare the initial state has also been outlined, and the impact of incoherent phenomena in realistic realizations has been addressed. In particular, the implementation with HgTe/CdTe QSHI proximized by Nb contacts is suggested to be promising, since decoherence effects due to Coulomb and hyperfine interactions are weak. Thus, the proposed realization of ASQ might foster interdisciplinary research across topological materials and quantum information.

ACKNOWLEDGMENTS

The authors greatly acknowledge interesting and inspiring discussions with F. Taddei, A. Braggio, A. Richaud, and A. Crippa. Financial support from the TOPMASQ ("Topological material platform for the implementation of Andreev spin qubit") project, a Cascade call project (CUP E13C24001560001) financed by the "National Quantum Science & Technology Institute," PE00000023 (Next Generation EU) is also acknowledged.

DATA AVAILABILITY

The data used to generate the figures of this manuscript are available at the Zenodo public repository [102].

APPENDIX: ABS WAVEFUNCTIONS

In this Appendix, we provide some details about the calculations of the ABS wavefunctions, which are needed to evaluate the electric dipole transition amplitudes in Eqs. (23) and (24) shown in Sec. III. Following the scheme of Ref. [71], we schematize the JJ as depicted in Fig. 10, where the weak link, sandwiched between the two superconductors S_L and S_R, can be regarded as a central scattering region characterized by the magnetic disorder, separated by ideal ballistic buffer normal regions N_L and N_R. While Andreev scattering occurs at the interfaces $x_L = -L/2$ and $x_R = +L/2$ of the weak link

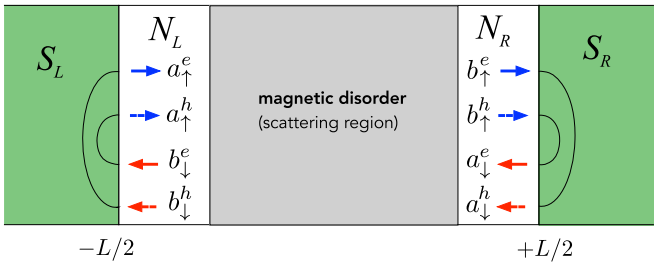

FIG. 10. Scheme of the JJ: Andreev scattering occurs at the interfaces $x_L = -L/2$ and $x_R = +L/2$, whereas the magnetic disorder inside the weak link induces normal scattering. The a symbols denote the amplitudes of states that are traveling from the S interfaces toward the magnetic disorder regions, while the b symbols denote the amplitudes of states traveling from the disordered region to the interfaces.

with the superconductors, normal scattering occurs because of magnetic disorder.

An eigenfunction $\Phi_E(x)$ of the BdG Hamiltonian (6) at energy E

$$\Phi_E(x) = \begin{pmatrix} u_{E\uparrow}(x) \\ u_{E\downarrow}(x) \\ v_{E\downarrow}(x) \\ v_{E\uparrow}(x) \end{pmatrix} \tag{A1}$$

can be constructed by combining the solutions in the various JJ regions depicted in Fig. 10. Specifically, because we are interested in the ABSs, i.e., in the subgap spectrum $0 \leqslant E \leqslant \Delta_0$, the expression of the wavefunction in the superconductors and in the buffer regions reads as follows.

Solutions in left superconductor S_L (subgap):

$$\Phi_E(x)|_{S_L} = \sqrt{\frac{\Delta_0}{2E}} \begin{pmatrix} f_- e^{-\frac{i}{2}\arccos\frac{E}{\Delta_0}} e^{iq_E^- x} \\ g_+ e^{\frac{i}{2}\arccos\frac{E}{\Delta_0}} e^{-iq_E^+ x} \\ f_- e^{+\frac{i}{2}\arccos\frac{E}{\Delta_0}} e^{iq_E^- x} e^{-i\phi_L} \\ g_+ e^{-\frac{i}{2}\arccos\frac{E}{\Delta_0}} e^{-iq_E^+ x} e^{-i\phi_L} \end{pmatrix}. \tag{A2}$$

Solutions in the left buffer region N_L:

$$\Phi_E(x)|_{N_L} = \begin{pmatrix} a^e_\uparrow e^{ik_E^e x} \\ b^e_\downarrow e^{-ik_E^e x} \\ b^h_\downarrow e^{ik_E^h x} \\ a^h_\uparrow e^{-ik_E^h x} \end{pmatrix}. \tag{A3}$$

Solutions in the right buffer region N_R:

$$\Phi_E(x)|_{N_R} = \begin{pmatrix} b^e_\uparrow e^{ik_E^e x} \\ a^e_\downarrow e^{-ik_E^e x} \\ a^h_\downarrow e^{ik_E^h x} \\ b^h_\uparrow e^{-ik_E^h x} \end{pmatrix}. \tag{A4}$$

Solution in the right superconductor S_R (subgap):

$$\Phi_E(x)|_{S_R} = \sqrt{\frac{\Delta_0}{2E}} \begin{pmatrix} f_+ e^{+\frac{i}{2}\arccos\frac{E}{\Delta_0}} e^{iq_E^+ x} \\ g_- e^{-\frac{i}{2}\arccos\frac{E}{\Delta_0}} e^{-iq_E^- x} \\ f_+ e^{-\frac{i}{2}\arccos\frac{E}{\Delta_0}} e^{iq_E^+ x} e^{-i\phi_R} \\ g_- e^{+\frac{i}{2}\arccos\frac{E}{\Delta_0}} e^{-iq_E^- x} e^{-i\phi_R} \end{pmatrix}. \tag{A5}$$

In the formulas here above, the symbols a, b, f, and g denote complex amplitudes, where their energy label E has been dropped to make the notation lighter. Moreover, $\phi_L = \phi/2$ and $\phi_R = -\phi/2$ are the superconducting phases in left and right superconductors, while

$$k_E^{e/h} = \frac{\mu \pm E}{\hbar v_F} \tag{A6}$$

denote the (real) wave vectors characterizing the normal buffer regions, and

$$q_E^\pm = \frac{1}{\hbar v_F}\left(\mu \pm i\sqrt{\Delta_0^2 - E^2}\right), \qquad 0 < E < \Delta_0, \tag{A7}$$

the (complex) wave vectors characterizing the decaying states in the superconducting regions $S_{L/R}$ in the subgap.

Imposing the continuity of the wavefunction at the left and right interfaces $x = x_L = -L/2$ and $x = x_R = +L/2$,

$$\Phi_E(x_L)|_{S_L} = \Phi_E(x_L)|_{N_L}, \tag{A8}$$

$$\Phi_E(x_R)|_{S_R} = \Phi_E(x_R)|_{N_R}, \tag{A9}$$

one obtains the coefficients characterizing the superconductor wavefunctions

$$f_-\sqrt{\frac{\Delta_0}{2E}} = a^e_\uparrow e^{\frac{i}{2}\arccos\frac{E}{\Delta_0}} e^{-iq_E^- x_L} e^{ik_E^e x_L}, \tag{A10}$$

$$f_+\sqrt{\frac{\Delta_0}{2E}} = a^h_\downarrow e^{\frac{i}{2}\arccos\frac{E}{\Delta_0}} e^{-iq_E^+ x_R} e^{ik_E^h x_R} e^{i\phi_R}, \tag{A11}$$

$$g_-\sqrt{\frac{\Delta_0}{2E}} = a^e_\downarrow e^{\frac{i}{2}\arccos\frac{E}{\Delta_0}} e^{iq_E^- x_R} e^{-ik_E^e x_R}, \tag{A12}$$

$$g_+\sqrt{\frac{\Delta_0}{2E}} = a^h_\uparrow e^{\frac{i}{2}\arccos\frac{E}{\Delta_0}} e^{iq_E^+ x_L} e^{-ik_E^h x_L} e^{i\phi_L}, \tag{A13}$$

as well as the Andreev reflection relations

$$b^e_\uparrow = a^h_\downarrow e^{i\arccos\frac{E}{\Delta_0}} e^{i\phi_R} e^{-i\frac{2Ex_R}{\hbar v_F}}, \tag{A14}$$

$$b^h_\uparrow = a^e_\downarrow e^{i\arccos\frac{E}{\Delta_0}} e^{-i\phi_R} e^{-i\frac{2Ex_R}{\hbar v_F}}, \tag{A15}$$

$$b^h_\downarrow = a^e_\uparrow e^{i\arccos\frac{E}{\Delta_0}} e^{-i\phi_L} e^{i\frac{2Ex_L}{\hbar v_F}}, \tag{A16}$$

$$b^e_\downarrow = a^h_\uparrow e^{i\arccos\frac{E}{\Delta_0}} e^{i\phi_L} e^{i\frac{2Ex_L}{\hbar v_F}}. \tag{A17}$$

At the same time, the magnetic disorder present in the JJ weak link induces normal scattering processes. In the electron sector, the scattering matrix S_e, which can be expressed as in Eq. (10), connects

$$\begin{pmatrix} b^e_\downarrow \\ b^e_\uparrow \end{pmatrix} = S_e(E) \begin{pmatrix} a^e_\uparrow \\ a^e_\downarrow \end{pmatrix}, \tag{A18}$$

whereas in the hole sector the scattering matrix $S_h(E)$, defined through

$$\begin{pmatrix} b^h_\downarrow \\ b^h_\uparrow \end{pmatrix} = S_h(E) \begin{pmatrix} a^h_\uparrow \\ a^h_\downarrow \end{pmatrix}, \tag{A19}$$

can be obtained from S_e through the relation (11). Thus, in the buffer regions N_L and N_R the outgoing amplitudes can be expressed in terms of the incoming ones as

$$b^e_\uparrow = t_e\, a^e_\uparrow + r'_e a^e_\downarrow, \tag{A20}$$

$$b^e_\downarrow = r_e\, a^e_\uparrow + t'_e a^e_\downarrow, \tag{A21}$$

$$b^h_\uparrow = t_h\, a^h_\uparrow + r'_h a^h_\downarrow, \tag{A22}$$

$$b^h_\downarrow = r_h\, a^h_\uparrow + t'_h a^h_\downarrow. \tag{A23}$$

Equating Eqs. (A14)–(A20) and Eqs. (A15)–(A22), one obtains

$$\begin{pmatrix} a^e_\uparrow \\ a^h_\uparrow \end{pmatrix} = A_R \begin{pmatrix} a^e_\downarrow \\ a^h_\downarrow \end{pmatrix}, \tag{A24}$$

where

$$A_R = \begin{pmatrix} -\frac{r'_e}{t_e} & \frac{1}{\alpha\, t_e} e^{i\phi_R} e^{-i\frac{2Ex_R}{\hbar v_F}} \\ \frac{1}{\alpha\, t_h} e^{-i\phi_R} e^{-i\frac{2Ex_R}{\hbar v_F}} & -\frac{r'_h}{t_h} \end{pmatrix} \tag{A25}$$

and

$$\alpha(E) = e^{-i \arccos \frac{E}{\Delta_0}}. \tag{A26}$$

Similarly, equating Eqs. (A17)–(A21) and Eqs. (A16)–(A23), one retrieves

$$\begin{pmatrix} a^e_\downarrow \\ a^h_\downarrow \end{pmatrix} = A_L \begin{pmatrix} a^e_\uparrow \\ a^h_\uparrow \end{pmatrix}, \tag{A27}$$

where

$$A_L = \begin{pmatrix} -\frac{r_e}{t'_e} & \frac{1}{\alpha\, t'_e} e^{i\phi_L} e^{i\frac{2Ex_L}{\hbar v_F}} \\ \frac{1}{\alpha\, t'_h} e^{-i\phi_L} e^{i\frac{2Ex_L}{\hbar v_F}} & -\frac{r_h}{t'_h} \end{pmatrix}. \tag{A28}$$

Combining Eqs. (A25) and (A28), one obtains

$$(\mathbb{I}_2 - A_R A_L) \begin{pmatrix} a^e_\uparrow \\ a^h_\uparrow \end{pmatrix} = \begin{pmatrix} 0 \\ 0 \end{pmatrix}, \tag{A29}$$

which has two important implications.

On the one hand, Eq. (A29) determines the equation $\det(\mathbb{I}_2 - A_L A_R) = 0$ of the discrete energy levels E_j characterizing the ABS wavefunctions $\Phi_E(x)$. Explicitly, using Eqs. (A25) and (A28), such an equation can be written as

$$\begin{aligned} &\alpha^{-2} e^{-2i\frac{E}{E_L}} + \alpha^2 e^{2i\frac{E}{E_L}} \det S^e(E) \det S^h(E) \\ &- (r'_e r'_h + r_e r_h) - e^{i\phi} t_e t'_h - e^{-i\phi} t_h t'_e = 0, \end{aligned} \tag{A30}$$

where $\phi = \phi_L - \phi_R$ and, from Eq. (11), one has

$$r_h(E) = -r^*_e(-E), \tag{A31}$$

$$t_h(E) = +t^*_e(-E), \tag{A32}$$

$$t'_h(E) = +t'^*_e(-E), \tag{A33}$$

$$r'_h(E) = -r'^*_e(-E). \tag{A34}$$

Exploiting the second expression in Eq. (10), one has $\det S^e(E) = -e^{2i\Gamma_m(E)}$ and $\det S^h(E) = -e^{-2i\Gamma_m(-E)}$. Moreover, using the definitions in Eq. (13), the ABS energy level equation (A30) reduces to Eq. (12), recovering the result of Ref. [64].

On the other hand, Eq. (A29) also implies

$$a^h_\uparrow = \frac{\alpha\, e^{i\frac{E}{E_L}} t'_h \det S_e(E) + \alpha^{-1} e^{-i\frac{E}{E_L}}\, e^{-i\phi}\, t'_e}{e^{-i\frac{\phi}{2}} r_h t'_e + e^{i\frac{\phi}{2}} r'_e t'_h}\, a^e_\uparrow, \tag{A35}$$

which can be substituted into the right-hand side of Eq. (A27), leading to obtain through a few algebra steps

$$a^e_\downarrow = \frac{\alpha^{-2} e^{-2i\frac{E}{E_L}} e^{-i\frac{\phi}{2}} - \left(e^{-i\frac{\phi}{2}} r_e r_h + e^{i\frac{\phi}{2}} t_e t'_h\right)}{e^{-i\frac{\phi}{2}} r_h t'_e + e^{i\frac{\phi}{2}} r'_e t'_h}\, a^e_\uparrow \tag{A36}$$

and

$$a^h_\downarrow = \frac{\alpha^{-1} e^{-i\frac{E}{E_L}} r'_e - \alpha\, e^{i\frac{E}{E_L}} r_h \det S_e}{e^{-i\frac{\phi}{2}} r_h t'_e + e^{i\frac{\phi}{2}} r'_e t'_h}\, a^e_\uparrow. \tag{A37}$$

Moreover, inserting Eqs. (A35)–(A37) into Eqs. (A14)–(A17), one finds

$$b^e_\uparrow = \frac{\alpha^{-2} e^{-2i\frac{E}{E_L}} r'_e - r_h \det S_e}{r_h t'_e + e^{i\phi} r'_e t'_h}\, a^e_\uparrow, \tag{A38}$$

$$\begin{aligned} b^h_\uparrow = {} & \frac{e^{+i\frac{\phi}{2}}\, e^{-i\frac{E}{E_L}}}{\alpha} \\ & \times \frac{\alpha^{-2} e^{-2i\frac{E}{E_L}} - (r_e r_h + e^{i\phi} t_e t'_h)}{r_h t'_e + e^{i\phi} r'_e t'_h}\, a^e_\uparrow, \end{aligned} \tag{A39}$$

$$b^h_\downarrow = \alpha^{-1}\, e^{-i\frac{\phi}{2}}\, e^{-i\frac{E}{E_L}}\, a^e_\uparrow, \tag{A40}$$

$$b^e_\downarrow = \frac{t'_h\, e^{i\phi} \det S_e(E) + \alpha^{-2} e^{-2i\frac{E}{E_L}}\, t'_e}{r_h t'_e + e^{i\phi} r'_e t'_h}\, a^e_\uparrow. \tag{A41}$$

Equations (A35)–(A41) express the seven coefficients $a^h_\uparrow$, $a^e_\downarrow$, $a^h_\downarrow$, $b^e_\uparrow$, $b^h_\uparrow$, $b^h_\downarrow$, and $b^e_\downarrow$ as a function of the coefficient $a^e_\uparrow$. Thus, inserting Eqs. (A35)–(A37) into Eqs. (A11)–(A13), the entire wavefunction in the superconductors and in the buffer regions can be expressed only in terms of the amplitude $a^e_\uparrow$ and the energy eigenvalue E_j found by solving Eq. (12). Moreover, also the wavefunction inside the magnetic domain can be expressed in terms of $a^e_\uparrow$, through relations that depend on the specific envisaged scatterer. Here below, we show how this is done in the illustrative example of a magnetic barrier. Thus, the entire wavefunction $\Phi_E(x)$ can be expressed in terms of $a^e_\uparrow$ only, which in turn is determined through the normalization condition $\int_{-\infty}^{+\infty} \Phi^\dagger_E(x)\Phi_E(x)\, dx = 1$.

1. Scattering matrix for a finite barrier

Because the magnetic disorder does not couple electron and hole sectors, one can determine the electron and hole

wavefunctions separately. Let us consider the case of a magnetic barrier

$$\mathbf{m}(x) = \begin{cases} 0, & x < x_1, \\ (m_\perp \cos\phi_\perp, m_\perp \sin\phi_\perp, m_z), & x_1 < x < x_2, \\ 0, & x < x_2, \end{cases} \tag{A42}$$

where $x_1 > -L/2$ and $x_2 < L/2$ are the magnetic domain boundaries within the weak link. This case generalizes Eq. (15) by including also a m_z component parallel to the natural quantization axis of the helical states, as well as a generic orientation $\phi_\perp$ within the spin x-y plane of the magnetization.

We focus on the electron sector, while a similar calculation can be carried out for the hole sector. The wavefunction in the clean buffer regions N_L and N_R reads

$$\begin{pmatrix} u_{E\uparrow}(x) \\ u_{E\downarrow}(x) \end{pmatrix} = \begin{pmatrix} a^e_\uparrow\, e^{+ik^e_E x} \\ b^e_\downarrow\, e^{-ik^e_E x} \end{pmatrix}, \qquad x < x_1 \tag{A43}$$

and

$$\begin{pmatrix} u_{E\uparrow}(x) \\ u_{E\downarrow}(x) \end{pmatrix} = \begin{pmatrix} b^e_\uparrow\, e^{+ik^e_E x} \\ a^e_\downarrow\, e^{-ik^e_E x} \end{pmatrix}, \qquad x > x_2, \tag{A44}$$

respectively, where k^e_E is given in Eq. (A6). For the wavefunction inside the barrier ($x_1 < x < x_2$), one has to distinguish two energy ranges. For $|\mu + E| < m_\perp$, the wavefunction consists of evanescent waves and reads

$$\begin{aligned} \begin{pmatrix} u_{E\uparrow}(x) \\ u_{E\downarrow}(x) \end{pmatrix} = {} & \frac{1}{\sqrt{2}} \begin{pmatrix} e^{+\frac{i}{2}(\tilde\theta^e_E - \phi_\perp)} \\ e^{-\frac{i}{2}(\tilde\theta^e_E - \phi_\perp)} \end{pmatrix} e^{+i\tilde k^{e+}_E x}\, c^e_+ \\ & + \frac{1}{\sqrt{2}} \begin{pmatrix} e^{-\frac{i}{2}(\tilde\theta^e_E + \phi_\perp)} \\ e^{+\frac{i}{2}(\tilde\theta^e_E + \phi_\perp)} \end{pmatrix} e^{+i\tilde k^{e-}_E x}\, c^e_-, \end{aligned} \tag{A45}$$

where $c^e_\pm$ are complex amplitudes,

$$\tilde k^{e\pm}_E = \frac{-m_z \pm i\sqrt{m_\perp^2 - (\mu+E)^2}}{\hbar v_F} \tag{A46}$$

are complex wave vectors, and $\tilde\theta^e_E$ is an angle such that

$$\cos\tilde\theta^e_E = \frac{\mu+E}{m_\perp}, \qquad \sin\tilde\theta^e_E = \frac{\sqrt{m_\perp^2 - (\mu+E)^2}}{m_\perp}. \tag{A47}$$

For $|\mu + E| > m_\perp$, the wavefunction exhibits an oscillatory behavior and is given by

$$\begin{aligned} \begin{pmatrix} u_{E\uparrow}(x) \\ u_{E\downarrow}(x) \end{pmatrix} = {} & \sqrt{\frac{m_\perp}{2|\mu+E|}} \begin{pmatrix} e^{+\frac{1}{2}(s_E\tilde\theta^e_E - i\phi_\perp)} \\ s_E e^{-\frac{1}{2}(s_E\tilde\theta^e_E - i\phi_\perp)} \end{pmatrix} e^{+i\bar k^{e+}_E x}\, c^e_+ \\ & + \sqrt{\frac{m_\perp}{2|\mu+E|}} \begin{pmatrix} e^{-\frac{1}{2}(s_E\tilde\theta^e_E + i\phi_\perp)} \\ s_E e^{+\frac{1}{2}(s_E\tilde\theta^e_E + i\phi_\perp)} \end{pmatrix} e^{+i\bar k^{e-}_E x}\, c^e_-, \end{aligned} \tag{A48}$$

where

$$\bar k^{e\pm}_E = \frac{-m_z \pm \sqrt{(\mu+E)^2 - m_\perp^2}}{\hbar v_F} \tag{A49}$$

are real wave vectors, and $\bar\theta^e_E$ is determined by

$$\cosh\bar\theta^e_E = \frac{|\mu+E|}{m_\perp}, \qquad \sinh\bar\theta^e_E = \frac{\sqrt{(\mu+E)^2 - m_\perp^2}}{m_\perp}, \tag{A50}$$

with $s_E = \mathrm{sgn}(\mu + E)$. Imposing the continuity at (say) the boundary x_1 of the wavefunctions in Eqs. (A43) and (A45) [or Eq. (A48)], one obtains a set of two linear equations that lead to express the amplitudes $c^e_\pm$ characterizing the wavefunction inside the magnetic region as a function of the amplitudes $a^e_\uparrow$ and $b^e_\downarrow$. The above calculations straightforwardly enable one to obtain the scattering matrix $S_e(E)$ of the barrier, which can be written in the form of Eq. (10), where the transmission coefficient is

$$T_E = \begin{cases} \left(1 + \left(\frac{m_\perp}{\sqrt{m_\perp^2 - (\mu+E)^2}} \sinh\left[\frac{L_m}{\hbar v_F}\sqrt{m_\perp^2 - (\mu+E)^2}\right]\right)^2\right)^{-1} & |\mu+E| < m_\perp, \\ \left(1 + \left(\frac{m_\perp}{\sqrt{(\mu+E)^2 - m_\perp^2}} \sin\left[\frac{L_m}{\hbar v_F}\sqrt{(\mu+E)^2 - m_\perp^2}\right]\right)^2\right)^{-1} & |\mu+E| > m_\perp, \end{cases} \tag{A51}$$

whereas the phases $\Gamma_m(E)$, $\Theta_m(E)$, and $\chi_m(E)$ are given by

$$\Gamma_m(E) = \begin{cases} \arctan\left[\frac{\mu+E}{\sqrt{m_\perp^2 - (\mu+E)^2}} \tanh\left(\frac{L_m}{\hbar v_F}\sqrt{m_\perp^2 - (\mu+E)^2}\right)\right] - \frac{(\mu+E)L_m}{\hbar v_F} & |\mu+E| < m_\perp, \\ \arctan\left[\frac{\mu+E}{\sqrt{(\mu+E)^2 - m_\perp^2}} \tan\left(\frac{L_m}{\hbar v_F}\sqrt{(\mu+E)^2 - m_\perp^2}\right)\right] - \frac{(\mu+E)L_m}{\hbar v_F} + & \\ \quad + \pi\,\vartheta\left[-\cos\left(\frac{L_m}{\hbar v_F}\sqrt{(\mu+E)^2 - m_\perp^2}\right)\right] & |\mu+E| > m_\perp, \end{cases} \tag{A52}$$

and

$$\Theta_m(E) = 2k^e_E x_0 + \phi_\perp, \tag{A53}$$

$$\chi_m(E) = \frac{m_z L_m}{\hbar v_F}, \tag{A54}$$

respectively. Here, $x_0 = (x_1 + x_2)/2$ denotes the midpoint of the barrier, $L_m = x_2 - x_1$ is its spatial extension, and ϑ is the Heaviside step function.

[1] N. M. Chtchelkatchev and Y. V. Nazarov, Andreev quantum dots for spin manipulation, Phys. Rev. Lett. **90**, 226806 (2003).

[2] C. Padurariu and Y. V. Nazarov, Theoretical proposal for superconducting spin qubits, Phys. Rev. B **81**, 144519 (2010).

[3] A. Zazunov, R. Egger, T. Jonckheere, and T. Martin, Anomalous Josephson current through a spin-orbit coupled quantum dot, Phys. Rev. Lett. **103**, 147004 (2009).

[4] A. A. Reynoso, G. Usaj, C. A. Balseiro, D. Feinberg, and M. Avignon, Spin-orbit-induced chirality of Andreev states in Josephson junctions, Phys. Rev. B **86**, 214519 (2012).

[5] M. Jakob, K. Laubscher, P. Vecchio, A. Chatterjee, V. Fatemi, and S. Bosco, Fast readout of quantum dot spin qubits via Andreev spins, arXiv:2506.19762.

[6] S. A. Wolf, D. D. Awschalom, R. A. Buhrman, J. M. Daughton, S. von Molnár, M. L. Roukes, A. Y. Chtchelkanova, and D. M. Treger, Spintronics: A spin-based electronics vision for the future, Science **294**, 1488 (2001).

[7] D. Awschalom and M. Flatté, Challenges for semiconductor spintronics, Nat. Phys. **3**, 153 (2007).

[8] H. Lu, I. A. Day, A. R. Akhmerov, B. van Heck, and V. Fatemi, Kramers-protected hardware-efficient error correction with Andreev spin qubits, Phys. Rev. Lett. **135**, 210602 (2025).

[9] S. Park and A. L. Yeyati, Andreev spin qubits in multichannel Rashba nanowires, Phys. Rev. B **96**, 125416 (2017).

[10] C. Metzger, S. Park, L. Tosi, C. Janvier, A. A. Reynoso, M. F. Goffman, C. Urbina, A. Levy-Yeyati, and H. Pothier, Circuit-QED with phase-biased Josephson weak links, Phys. Rev. Res. **3**, 013036 (2021).

[11] Y. Fauvel, J. S. Meyer, and M. Houzet, Opportunities for the direct manipulation of a phase-driven Andreev spin qubit, Phys. Rev. B **109**, 184515 (2024).

[12] L. Tosi, C. Metzger, M. F. Goffman, C. Urbina, H. Pothier, S. Park, A. L. Yeyati, J. Nygård, and P. Krogstrup, Spin-orbit splitting of Andreev states revealed by microwave spectroscopy, Phys. Rev. X **9**, 011010 (2019).

[13] M. Hays, V. Fatemi, K. Serniak, D. Bouman, S. Diamond, G. Lange, P. Krogstrup, J. Nygård, A. Geresdi, and M. Devoret, Continuous monitoring of a trapped superconducting spin, Nat. Phys. **16**, 1103 (2020).

[14] M. Hays, V. Fatemi, D. Bouman, J. Cerrillo, S. Diamond, K. Serniak, T. Connolly, P. Krogstrup, J. Nygård, A. L. Yeyati, A. Geresdi, and M. H. Devoret, Coherent manipulation of an Andreev spin qubit, Science **373**, 430 (2021).

[15] M. Pita-Vidal, A. Bargerbos, R. Žitko, L. Splitthoff, L. Grünhaupt, J. Wesdorp, Y. Liu, L. Kouwenhoven, R. Aguado, B. Heck, A. Kou, and C. Andersen, Direct manipulation of a superconducting spin qubit strongly coupled to a transmon qubit, Nat. Phys. **19**, 1110 (2023).

[16] A. Bargerbos, M. Pita-Vidal, R. Žitko, L. J. Splitthoff, L. Grünhaupt, J. J. Wesdorp, Y. Liu, L. P. Kouwenhoven, R. Aguado, C. K. Andersen, A. Kou, and B. van Heck, Spectroscopy of spin-split Andreev levels in a quantum dot with superconducting leads, Phys. Rev. Lett. **131**, 097001 (2023).

[17] M. Pita-Vidal, J. J. Wesdorp, L. J. Splitthoff, A. Bargerbos, Y. Liu, L. P. Kouwenhoven, and C. K. Andersen, Strong tunable coupling between two distant superconducting spin qubits, Nat. Phys. **20**, 1158 (2024).

[18] M. Pita-Vidal, J. J. Wesdorp, and C. K. Andersen, Blueprint for all-to-all-connected superconducting spin qubits, PRX Quantum **6**, 010308 (2025).

[19] H. Lu, D. F. Bofill, Z. Sun, T. Kanne, J. Nygård, M. Kjaergaard, and V. Fatemi, Andreev spin relaxation time in a shadow-evaporated InAs weak link, Phys. Rev. Appl. **24**, 024046 (2025).

[20] S. Hoffman, M. Hays, K. Serniak, T. Hazard, and C. Tahan, Decoherence in Andreev spin qubits, Phys. Rev. B **111**, 045304 (2025).

[21] S. Hoffman and C. Tahan, Resolving Andreev spin qubits in Germanium-based Josephson junctions, arXiv:2506.13988.

[22] M. Valentini, O. Sagi, L. Baghumyan, T. Gijsel, J. Jung, S. Calcaterra, A. Ballabio, J. Aguilera, K. Aggarwal, M. Janík, T. Adletzberger, R. Seoane Souto, M. Leijnse, J. Danon, C. Schrade, E. Bakkers, D. Chrastina, G. Isella, and G. Katsaros, Parity-conserving Cooper-pair transport and ideal superconducting diode in planar germanium, Nat. Commun. **15**, 169 (2024).

[23] A. Leblanc, C. Tangchingchai, Z. Sadre Momtaz, E. Kiyooka, J.-M. Hartmann, F. Gustavo, J.-L. Thomassin, B. Brun, V. Schmitt, S. Zihlmann, R. Maurand, E. Dumur, S. De Franceschi, and F. Lefloch, Gate- and flux-tunable $\sin(2\phi)$ Josephson element with planar-Ge junctions, Nat. Commun. **16**, 1010 (2025).

[24] P. D. Kurilovich, T. Vakhtel, T. Connolly, C. G. L. Bøttcher, and B. van Heck, Andreev spin qubit protected by Franck-Condon blockade, Phys. Rev. B **113**, 115429 (2026).

[25] K. Laubscher, V. Fatemi, and J. Sau, Andreev spin qubits bound to Josephson vortices in spin-orbit coupled planar Josephson junctions, arXiv:2512.11021.

[26] A. Svetogorov, K. Piasotski, W. Belzig, and M. Pletyukhov, Theory of three-terminal Andreev spin qubits, Phys. Rev. B **112**, L100508 (2025).

[27] P. San-Jose and E. Prada, Solitonic Andreev spin qubits from Andreev states in Corbino Josephson junctions, Phys. Rev. Res. **8**, 013076 (2026).

[28] B. A. Bernevig and S.-C. Zhang, Quantum spin Hall effect, Phys. Rev. Lett. **96**, 106802 (2006).

[29] M. König, H. Buhmann, L. W. Molenkamp, T. Hughes, C.-X. Liu, X.-L. Qi, and S.-C. Zhang, The quantum spin Hall effect: Theory and experiment, J. Phys. Soc. Jpn. **77**, 031007 (2008).

[30] X.-L. Qi and S.-C. Zhang, Topological insulators and superconductors, Rev. Mod. Phys. **83**, 1057 (2011).

[31] Y. Ando, Topological insulator materials, J. Phys. Soc. Jpn. **82**, 102001 (2013).

[32] B. A. Bernevig, T. L. Hughes, and S.-C. Zhang, Quantum spin Hall effect and topological phase transition in HgTe quantum wells, Science **314**, 1757 (2006).

[33] M. König, S. Wiedmann, C. Brüne, A. Roth, H. Buhmann, L. W. Molenkamp, X.-L. Qi, and S.-C. Zhang, Quantum spin Hall insulator state in HgTe quantum wells, Science **318**, 766 (2007).

[34] C. Brüne, A. Roth, E. G. Novik, M. König, H. Buhmann, E. M. Hankiewicz, W. Hanke, J. Sinova, and L. W. Molenkamp, Evidence for the ballistic intrinsic spin Hall effect in HgTe nanostructures, Nat. Phys. **6**, 448 (2010).

[35] K. Nowack, E. Spanton, M. Baenninger, M. König, J. Kirtley, B. Kalisky, C. Ames, P. Leubner, C. Brüne, H. Buhmann, L. Molenkamp, D. Goldhaber-Gordon, and K. Moler, Imaging currents in HgTe quantum wells in the quantum spin Hall regime, Nat. Mater. **12**, 787 (2013).

[36] I. Knez, R.-R. Du, and G. Sullivan, Evidence for helical edge modes in inverted InAs/GaSb quantum wells, Phys. Rev. Lett. **107**, 136603 (2011).

[37] L. Du, I. Knez, G. Sullivan, and R.-R. Du, Robust helical edge transport in gated InAs/GaSb bilayers, Phys. Rev. Lett. **114**, 096802 (2015).

[38] S. Murakami, Quantum spin Hall effect and enhanced magnetic response by spin-orbit coupling, Phys. Rev. Lett. **97**, 236805 (2006).

[39] I. Drozdov, A. Alexandradinata, S. Jeon, S. Nadj-Perge, H. Ji, R. Cava, B. Bernevig, and A. Yazdani, One-dimensional topological edge states of Bismuth bilayers, Nat. Phys. **10**, 664 (2014).

[40] G. Li and S. Wang, Quantum spin Hall states in 2D Bismuth-based materials, Springer Ser. Mater. Sci. **285**, 351 (2019).

[41] Z. Fei, T. Palomaki, S. Wu, W. Zhao, X. Cai, B. Sun, P. Nguyen, J. Finney, X. Xu, and D. Cobden, Edge conduction in monolayer WTe_2, Nat. Phys. **13**, 677 (2017).

[42] S. Tang, *et al.*, Quantum spin Hall state in monolayer 1T'-WTe_2, Nat. Phys. **13**, 683 (2017).

[43] S. Wu, V. Fatemi, Q. D. Gibson, K. Watanabe, T. Taniguchi, R. J. Cava, and P. Jarillo-Herrero, Observation of the quantum spin Hall effect up to 100 Kelvin in a monolayer crystal, Science **359**, 76 (2018).

[44] J. C. Budich, F. Dolcini, P. Recher, and B. Trauzettel, Phonon-induced backscattering in helical edge states, Phys. Rev. Lett. **108**, 086602 (2012).

[45] C.-H. Hsu, P. Stano, J. Klinovaja, and D. Loss, Helical liquids in semiconductors, Semicond. Sci. Technol. **36**, 123003 (2021).

[46] A. M. Lunde and G. Platero, Helical edge states coupled to a spin bath: Current-induced magnetization, Phys. Rev. B **86**, 035112 (2012).

[47] A. Del Maestro, T. Hyart, and B. Rosenow, Backscattering between helical edge states via dynamic nuclear polarization, Phys. Rev. B **87**, 165440 (2013).

[48] C.-H. Hsu, P. Stano, J. Klinovaja, and D. Loss, Nuclear-spin-induced localization of edge states in two-dimensional topological insulators, Phys. Rev. B **96**, 081405(R) (2017).

[49] C.-H. Hsu, P. Stano, J. Klinovaja, and D. Loss, Effects of nuclear spins on the transport properties of the edge of two-dimensional topological insulators, Phys. Rev. B **97**, 125432 (2018).

[50] S. Hart, H. Ren, T. Wagner, P. Leubner, M. Mühlbauer, C. Brüne, H. Buhmann, L. W. Molenkamp, and A. Yacoby, Induced superconductivity in the quantum spin Hall edge, Nat. Phys. **10**, 638 (2014).

[51] V. Pribiag, A. Beukman, F. Qu, M. Cassidy, C. Charpentier, W. Wegscheider, and L. Kouwenhoven, Edge-mode superconductivity in a two-dimensional topological insulator, Nat. Nanotechnol. **10**, 593 (2015).

[52] J. Wiedenmann, E. Bocquillon, R. Deacon, S. Hartinger, O. Herrmann, T. Klapwijk, L. Maier, C. Ames, C. Brüne, C. Gould, A. Oiwa, K. Ishibashi, S. Tarucha, H. Buhmann, and L. Molenkamp, 4π-periodic Josephson supercurrent in HgTe-based topological Josephson junctions, Nat. Commun. **7**, 10303 (2016).

[53] E. Bocquillon, R. S. Deacon, J. Wiedenmann, P. Leubner, T. M. Klapwijk, C. Brüne, K. Ishibashi, H. Buhmann, and L. W. Molenkamp, Gapless Andreev bound states in the quantum spin Hall insulator HgTe, Nat. Nanotechnol. **12**, 137 (2017).

[54] P. Mandal, S. Mondal, M. Stehno, S. Ilić, F. Bergeret, T. Klapwijk, C. Gould, and L. Molenkamp, Magnetically tunable supercurrent in dilute magnetic topological insulator-based Josephson junctions, Nat. Phys. **20**, 984 (2024).

[55] W. Liu, S. Piatrusha, X. Liang, S. Upadhyay, L. Fürst, C. Gould, J. Kleinlein, H. Buhmann, M. Stehno, and L. Molenkamp, Period-doubling in the phase dynamics of a shunted HgTe quantum well Josephson junction, Nat. Commun. **16**, 3068 (2025).

[56] S. Artemenko and V. Kaladzhyan, Photogalvanic effects in topological insulators, JETP Lett. **97**, 82 (2013).

[57] B. Dóra, J. Cayssol, F. Simon, and R. Moessner, Optically engineering the topological properties of a spin Hall insulator, Phys. Rev. Lett. **108**, 056602 (2012).

[58] F. Dolcini, R. C. Iotti, A. Montorsi, and F. Rossi, Photoexcitation of electron wave packets in quantum spin Hall edge states: Effects of chiral anomaly from a localized electric pulse, Phys. Rev. B **94**, 165412 (2016).

[59] G. Dolcetto, F. Cavaliere, and M. Sassetti, Magnetic ac control of the spin textures in a helical Luttinger liquid, Phys. Rev. B **89**, 125419 (2014).

[60] B. Jäck, Y. Xie, B. A. Bernevig, and A. Yazdani, Observation of backscattering induced by magnetism in a topological edge state, Proc. Natl. Acad. Sci. USA **117**, 16214 (2020).

[61] S. Shamim, W. Beugeling, P. Shekhar, K. Bendias, L. Lunczer, J. Kleinlein, H. Buhmann, and L. Molenkamp, Quantized spin Hall conductance in a magnetically doped two dimensional topological insulator, Nat. Commun. **12**, 3193 (2021).

[62] C.-X. Liu, X.-L. Qi, X. Dai, Z. Fang, and S.-C. Zhang, Quantum anomalous Hall effect in $Hg_{1-y}Mn_yTe$ quantum wells, Phys. Rev. Lett. **101**, 146802 (2008).

[63] S.-G. Cheng, The quantum anomalous Hall effect in a topological insulator thin film—The role of magnetic disorder, Europhys. Lett. **105**, 57004 (2014).

[64] F. Crépin, B. Trauzettel, and F. Dolcini, Signatures of Majorana bound states in transport properties of hybrid structures based on helical liquids, Phys. Rev. B **89**, 205115 (2014).

[65] C. Wu, B. A. Bernevig, and S.-C. Zhang, Helical liquid and the edge of quantum spin Hall systems, Phys. Rev. Lett. **96**, 106401 (2006).

[66] J. Maciejko, C. Liu, Y. Oreg, X.-L. Qi, C. Wu, and S.-C. Zhang, Kondo effect in the helical edge liquid of the quantum spin Hall state, Phys. Rev. Lett. **102**, 256803 (2009).

[67] Y. Tanaka, A. Furusaki, and K. A. Matveev, Conductance of a helical edge liquid coupled to a magnetic impurity, Phys. Rev. Lett. **106**, 236402 (2011).

[68] E. Eriksson, A. Ström, G. Sharma, and H. Johannesson, Electrical control of the Kondo effect in a helical edge liquid, Phys. Rev. B **86**, 161103 (2012).

[69] B. L. Altshuler, I. L. Aleiner, and V. I. Yudson, Localization at the edge of a 2D topological insulator by Kondo impurities with random anisotropies, Phys. Rev. Lett. **111**, 086401 (2013).

[70] J.-H. Zheng and M. A. Cazalilla, Nontrivial interplay of strong disorder and interactions in quantum spin-Hall insulators doped with dilute magnetic impurities, Phys. Rev. B **97**, 235402 (2018).

[71] C. W. J. Beenakker, Universal limit of critical-current fluctuations in mesoscopic Josephson junctions, Phys. Rev. Lett. **67**, 3836 (1991).

[72] P. F. Bagwell, Suppression of the Josephson current through a narrow, mesoscopic, semiconductor channel by a single impurity, Phys. Rev. B **46**, 12573 (1992).

[73] C. W. J. Beenakker and H. van Houten, Josephson current through a superconducting quantum point contact shorter than the coherence length, Phys. Rev. Lett. **66**, 3056 (1991).

[74] C. Ishii, Josephson currents through junctions with normal metal barriers, Prog. Theor. Phys. **44**, 1525 (1970).

[75] H.-J. Kwon, K. Sengupta, and V. Yakovenko, Fractional ac Josephson effect in p- and d-wave superconductors, Eur. Phys. J. B **37**, 349 (2003).

[76] L. Fu and C. L. Kane, Josephson current and noise at a superconductor/quantum-spin-Hall-insulator/superconductor junction, Phys. Rev. B **79**, 161408 (2009).

[77] C. W. J. Beenakker, D. I. Pikulin, T. Hyart, H. Schomerus, and J. P. Dahlhaus, Fermion-parity anomaly of the critical supercurrent in the quantum spin-Hall effect, Phys. Rev. Lett. **110**, 017003 (2013).

[78] S. Barbarino, R. Fazio, M. Sassetti, and F. Taddei, Parity dependent Josephson current through a helical Luttinger liquid, New J. Phys. **15**, 085025 (2013).

[79] F. Crépin and B. Trauzettel, Parity measurement in topological Josephson junctions, Phys. Rev. Lett. **112**, 077002 (2014).

[80] A. Calzona and B. Trauzettel, Spin-resolved spectroscopy of helical Andreev bound states, Phys. Rev. Res. **4**, 013182 (2022).

[81] F. Rossi, *Theory of Semiconductor Quantum Devices: Microscopic Modeling and Simulation Strategies* (Springer, Berlin, Heidelberg, 2011).

[82] M. A. Nielsen and I. L. Chuang, *Quantum Computation and Quantum Information* (Cambridge University Press, Cambridge, 2010).

[83] F. Lüpke, D. Waters, S. de la Barrera, M. Widom, D. Mandrus, J.-Q. Yan, R. Feenstra, and B. Hunt, Proximity-induced superconducting gap in the quantum spin Hall edge state of monolayer WTe_2, Nat. Phys. **16**, 526 (2020).

[84] D. Frombach and P. Recher, Quasiparticle poisoning effects on the dynamics of topological Josephson junctions, Phys. Rev. B **101**, 115304 (2020).

[85] A. E. Svetogorov, D. Loss, and J. Klinovaja, Quasiparticle poisoning in trivial and topological Josephson junctions, Phys. Rev. B **105**, 174519 (2022).

[86] J. Berezovsky, M. H. Mikkelsen, N. G. Stoltz, L. A. Coldren, and D. D. Awschalom, Picosecond coherent optical manipulation of a single electron spin in a quantum dot, Science **320**, 349 (2008).

[87] D. Press, T. Ladd, B. Zhang, and Y. Yamamoto, Complete quantum control of a single quantum dot spin using ultrafast optical pulses, Nature (London) **456**, 218 (2008).

[88] K. D. Greve, D. Press, P. L. McMahon, and Y. Yamamoto, Ultrafast optical control of individual quantum dot spin qubits, Rep. Prog. Phys. **76**, 092501 (2013).

[89] Y. Makhlin, G. Schön, and A. Shnirman, Quantum-state engineering with Josephson-junction devices, Rev. Mod. Phys. **73**, 357 (2001).

[90] M. Devoret and J. Martinis, Implementing qubits with superconducting integrated circuits: Experimental aspects of quantum computing, Quantum Info. Proc. **3**, 163 (2004).

[91] G. Wendin and V. Shumeiko, Quantum bits with Josephson junctions (review article), Low Temp. Phys. **33**, 724 (2007).

[92] L. Chirolli and G. Burkard, Decoherence in solid-state qubits, Adv. Phys. **57**, 225 (2008).

[93] G. Burkard, T. D. Ladd, A. Pan, J. M. Nichol, and J. R. Petta, Semiconductor spin qubits, Rev. Mod. Phys. **95**, 025003 (2023).

[94] I. A. Merkulov, A. L. Efros, and M. Rosen, Electron spin relaxation by nuclei in semiconductor quantum dots, Phys. Rev. B **65**, 205309 (2002).

[95] T. Li, P. Wang, H. Fu, L. Du, K. A. Schreiber, X. Mu, X. Liu, G. Sullivan, G. A. Csáthy, X. Lin, and R.-R. Du, Observation of a helical Luttinger liquid in InAs/GaSb quantum spin Hall edges, Phys. Rev. Lett. **115**, 136804 (2015).

[96] J. C. Y. Teo and C. L. Kane, Critical behavior of a point contact in a quantum spin Hall insulator, Phys. Rev. B **79**, 235321 (2009).

[97] A. Ström and H. Johannesson, Tunneling between edge states in a quantum spin Hall system, Phys. Rev. Lett. **102**, 096806 (2009).

[98] J. Strunz, J. Wiedenmann, C. Fleckenstein, L. Lunczer, W. Beugeling, V. Müller, P. Shekhar, N. Traverso Ziani, S. Shamim, J. Kleinlein, H. Buhmann, B. Trauzettel, and L. Molenkamp, Interacting topological edge channels, Nat. Phys. **16**, 83 (2020).

[99] R. Fazio, F. W. J. Hekking, and A. A. Odintsov, Josephson current through a Luttinger liquid, Phys. Rev. Lett. **74**, 1843 (1995).

[100] R. Fazio, F. W. J. Hekking, and A. A. Odintsov, dc and ac Josephson effect in a superconductor–Luttinger-liquid–superconductor system, Phys. Rev. B **53**, 6653 (1996).

[101] D. L. Maslov, M. Stone, P. M. Goldbart, and D. Loss, Josephson current and proximity effect in Luttinger liquids, Phys. Rev. B **53**, 1548 (1996).

[102] E. Latini, F. Rossi, and F. Dolcini, Andreev spin qubits based on the helical edge states of magnetically doped two-dimensional topological insulators, Zenodo, 2026, https://zenodo.org/records/20580734.